Acta Materialia 175 (2019) 222–237

Contents lists available at ScienceDirect

Acta Materialia

journal homepage: www.elsevier.com/locate/actamat

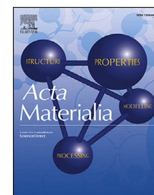

Full length article

Hot carrier transfer and phonon transport in suspended nm WS_2 films

Hamidreza Zobeiri [a, 1], Ridong Wang [a, 1], Qianying Zhang [b], Guangjun Zhu [b, **], Xinwei Wang [a, *]

[a] Department of Mechanical Engineering, Iowa State University, Ames, IA, 50011, United States
[b] College of Metallurgy and Material Engineering, Chongqing University of Science & Technology, University Town, Huxi Shapingba District, Chongqing, 401331, PR China

ARTICLE INFO

Article history:
Received 15 March 2019
Received in revised form
7 June 2019
Accepted 7 June 2019
Available online 12 June 2019

Keywords:
Raman spectroscopy
Thermal conductivity
Transport properties
Semiconductors
nm-thick WS_2

ABSTRACT

This work reports the first results on the conjugated hot carrier diffusivity (D) and thermal conductivity (κ) of suspended nm-thick WS_2 structures. A novel nET-Raman technique is developed to distinguish and characterize these two properties by constructing steady and transient states of different laser heating and Raman probing sizes. The nET-Raman uses a nanosecond pulsed laser and a continuous wave laser for exciting Raman signals and heating samples. κ is found to increase from $15.1^{+0.3}_{-0.4}$ to $38.8^{+2.6}_{-2.4}$ $W \cdot m^{-1} K^{-1}$ when the sample's thickness increases from 13 to 107 nm. This increase is attributed to the decreased effect of surface phonon scattering in thicker samples. Also, hot carrier diffusion length (Δr_{HC}) for these samples are measured without knowledge of hot carrier's lifetime (τ). Measured D of these four samples are in close range (except the thickest sample). This is due to the fact that lattice scattering for all these samples is similar and there is no substrate effect on our suspended films. nET-Raman is very robust and has negligible effect from laser absorption depth, sample thickness, and laser spot drift during measurement.

© 2019 Acta Materialia Inc. Published by Elsevier Ltd. All rights reserved.

1. Introduction

Two dimensional (2D) materials, especially graphene and graphene like materials, have been topics of extensive recent research [1–6]. Among 2D materials, Thin layers of transition metal dichalcogenides (TMDs) have attracted great interest due to their distinctive electrical and thermal properties, such as tunable bandgap [7,8], strong photoluminescence [9], and large exciton binding energy [10]. There are various applications for these unique properties, like solar cells [11,12], photodetectors [13,14], and field-effect transistors [15,16]. As a result, it is important to characterize their thermal and electrical properties at the nanoscale to optimize the performance of aforementioned devices.

Heat and electrical transport phenomena in nanoscale are mostly controlled by hot carrier properties, thermal conductivity of material, and interfacial thermal resistance between the thin film and substrate. In semiconductors, hot carriers are hot electrons or holes which have gained excess amount of energy over the Fermi energy. These carriers can be generated optically by photons with large amount of energy. The carrier diffusion coefficient (D) is used to describe the carrier movement in this environment. Study of hot carrier transport is important because it can provide us information about the scattering processes in semiconductors, such as exciton interactions, electron-electron collision, electron-phonon coupling, *etc* [17]. To date, several groups have developed techniques to investigate the hot carrier transport properties under high electric field or photon-injection [18–21]. However little optical studies have been reported. In comparison with optical methods, using the high electric field or photon injection method, ultrathin samples are more likely to be modified or destroyed during device preparation [22,23]. To date, little studies based on optical methods are reported for TMDs. Kumar et al. used a transient absorption microscopy method to study charge carrier dynamics in bulk MoS_2. By monitoring the spatiotemporal dynamics of hot carriers, they measured a diffusion coefficient of 4.2 $cm^2 s^{-1}$ [24]. Wang et al. reported a study of charge carriers in atomically thin MoS_2 sample which are supported on Si substrate, and obtained diffusion coefficient of 20 $cm^2 s^{-1}$ [25]. He et al. studied the spatiotemporal dynamics of excitons in both monolayer and bulk WS_2 samples on Si by transient absorption microscopy in the reflection geometry and

* Corresponding author.
** Corresponding author.
E-mail addresses: zhugjun@163.com (G. Zhu), xwang3@iastate.edu (X. Wang).
[1] H. Zobeiri and R. Wang contributed equally to this work.

https://doi.org/10.1016/j.actamat.2019.06.011
1359-6454/© 2019 Acta Materialia Inc. Published by Elsevier Ltd. All rights reserved.

determined D of monolayer and bulk WS_2 as 60 and 3.5 $cm^2\,s^{-1}$, respectively [26]. Most of the previous work are conducted for supported TMD thin layers, while no work has been conducted for suspended samples.

In the work previously done by our group, Yuan et al. determined the hot carrier diffusion coefficient (D) and interfacial thermal resistance (R) of very thin (less than 10 nm) exfoliated MoS_2 films on Si [27]. They investigated the effects of photon excitation, diffusion, and recombination by varying the heating spot size and probing the local temperature rise using Raman spectroscopy. Finally, in order to find D and R, they measured the temperature rise of the MoS_2 thin film and c-Si substrate based on the determined laser power coefficient and Raman temperature coefficient [27]. In next step, they developed energy transport state resolved Raman (ET-Raman) technique to simultaneously determine D and R [28]. Using this technique, they could eliminate the large errors introduced by laser absorption evaluation and Raman temperature coefficient calibration. ET-Raman is based on two energy transport states: steady state using a continuous wave (CW) laser and near zero-transport state generated by a picosecond (ps) pulsed laser. Under different heating spot sizes and these two energy transport states, they could determine D and R of MoS_2 thin films in the range of 6.6–17.4 nm supported on c-Si by comparing Raman shift variations of each of these states in both time and space domains. In another work conducted by our group, Yuan et al. measured the in-plane κ of supported few-layered (FL) MoS_2, as well as D and R, simultaneously [29]. The FL MoS_2 thin layers were supported on a glass substrate, instead of c-Si. Since c-Si is much more capable to dissipate heat than glass, they could investigate the effects of substrate on this study. By using a five-state ET-Raman technique, they successfully considered effects of D and R in the κ measurement. However, ET-Raman using a picosecond laser could only be implemented on supported samples and not suspended ones. To prevent significant heat accumulation caused by very short laser pulse generated by picosecond laser, Wang et al. further developed the ET-Raman technique and conducted the experiment by using a nanosecond laser instead of ps laser [30]. Using this new nET-Raman technique, since the laser pulse width is in the order of nanoseconds, they could determine in-plane κ of suspended MoS_2 and $MoSe_2$ samples without damaging the film. Measured thermal conductivity of four MoS_2 and $MoSe_2$ samples with different thicknesses are compared with the results of ten other works and are in very good agreement with them. In ET-Raman, nET-Raman, and FET-Raman [31] techniques which are developed by our group, only one laser in each heating state is used to heat the sample and probe the Raman signal. While in works conducted by other groups two lasers are used: one for heating the sample, and one as a probe for the Raman spectroscopy measurement [32].

Using other techniques, other groups measured κ of suspended samples. Peimyoo et al. reported the thermal conductivity of suspended monolayer and bilayer WS_2 sample by using of temperature and excitation dependence of WS_2 Raman peaks. The measured thermal conductivity is 32 and 53 $W\,m^{-1}\,K^{-1}$ for monolayer and bilayer samples [33]. In another work, Yan et al. obtained thermal conductivity of suspended monolayer MoS_2 from temperature-dependent Raman spectroscopy [34]. Additionally, Sahoo et al. conducted a temperature-dependent Raman study using suspended few-layered MoS_2 samples and measured κ at room temperature as 52 $W\,m^{-1}\,K^{-1}$ [35]. In all of these works or similar works, hot carriers' effect is not considered in measurement of κ of suspended samples. On the other hand, as mentioned above, hot carrier diffusion could affect the performance of electrical devices significantly and needs to be considered. In addition, majority of the previous works are done on MoS_2 samples, and WS_2 remains rarely explored, while WS_2 possesses the highest photoluminescence (PL) and excellent charge transport performance among all TMDs [36,37].

In this work, we measure and distinguish the thermal conductivity and hot carrier diffusivity of nm-thick suspended WS_2 films. To do so, we develop a 3-state nanosecond ET-Raman technique (nET-Raman) with energy transport variations in both time and space domains. By conducting this measurement, we characterize the intrinsic hot carrier transport properties of WS_2 nm-thick films without exposing the sample to an electric field or making any electrical contact. Also, by conducting the technique on suspended films, any effect of substrate on hot carrier diffusivity is eliminated. Additionally, the large errors caused by laser absorption coefficient and Raman temperature coefficient calibration are eliminated by this novel nET-Raman technique. In the following, the feasibility of this technique is also explored in detail. Its accuracy, capability, and measurement scope are studied to provide full assessment of its measurement capacity.

2. Physical principles

Fig. 1 shows the physics explored in our technique. Steady state continuous-wave or nanosecond lasers with 532 nm wavelength (with photon energy of $E = 2.33$ eV) irradiates the suspended sample. This excitation energy (E) is more than the bandgap of WS_2 samples ($E_g \approx 1.4$ eV) [38,39] and is enough to excite electrons (e) from the valence band to conduction band, while holes (h) remain in the valence band.

Excited electrons with a higher energy than bandgap release the excessive amount of their energy ($E - E_g$) through a non-radiative direct phonon emission. This process takes place in a very short time (in order of ps) [40], so it is reasonable to neglect the hot carrier diffusion effects during it. After this process, hot electrons and holes (hot carriers) diffuse, recombine and release the remained amount of photon energy (E_g). Due to conservation of crystal momentum and indirect bandgap of few-layered WS_2 thin layers, e-h pairs recombine via a non-radiative process. This recombination process happens in a longer time (order of nanoseconds) [26,41,42] in comparison with the fast thermalization process and leads to a wider thermal source spatial redistribution and needs to be finely considered in our study. Therefore, two main processes happen: (1) hot e-h generation, diffusion in space domain, and e-h recombination, and (2) heat conduction by phonons that receive their energy from hot carriers in process (1). The first one depends mostly on hot carrier diffusivity (D), while the second process is determined by the in-plane thermal conductivity of the sample (κ). Finally, phonons reach thermal equilibrium with electrons.

In this technique, we construct two heat transport states in both time and space domains to investigate hot carrier and thermal transports. The first energy transport state is steady state. Fig. 2(a) show a suspended sample under irradiation of a CW laser using a 20 × objective lens to construct this state. The laser spot radius in this case is around 1.6 μm (e^{-1} peak value). By varying the laser power under this heating state, we obtain the Raman shift power coefficient (RSC) value, which is defined as: $\psi_{CW} = \partial\omega/\partial P$. ψ_{CW} is function of κ, D, laser absorption coefficient (α), and Raman temperature coefficient [Fig. 2(c)]. During this heating process, WS_2 nanosheets absorb the laser energy and conduct it in both in-plane and out-of-plane directions via its thermal conductivity: $\kappa_{\parallel}$ and $\kappa_{\perp}$, respectively. As it will be mentioned in the following parts, we can assume that temperature distribution in the thickness direction is uniform due to the very thin film thickness, volumetric laser absorption, and relatively short heat conduction time in the thickness direction (shorter than the ns laser pulse width).

The second thermal transport state is constructed using a nanosecond pulsed laser (ns laser) with 300 kHz frequency

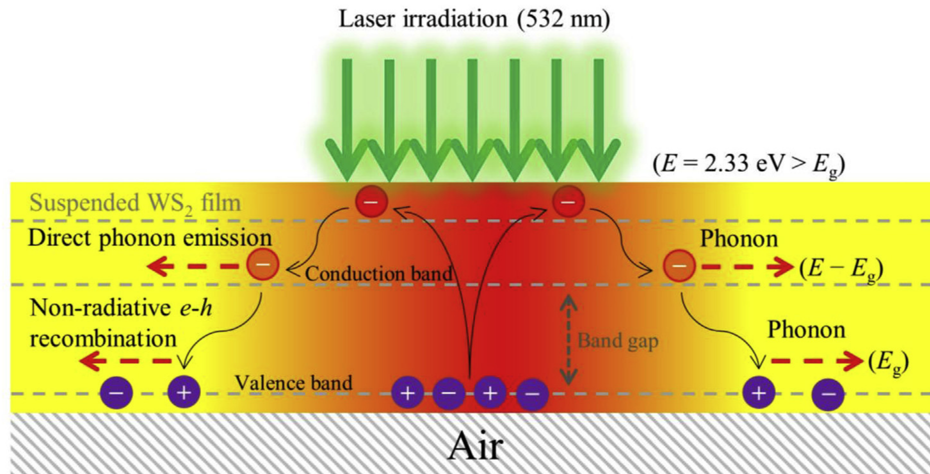

Fig. 1. Physical model of hot carrier generation, diffusion, and recombination under laser irradiation. A 532 nm wavelength laser ($E = 2.33$ eV) irradiates the suspended sample and excites the electrons in valence band to conduction band, while holes remain in valence band. Hot electrons in conduction band release some part of their energy ($E - E_g$) via a fast thermalization process (in order of ps). Next, the hot electrons with energy of E_g recombine with holes through a non-radiative process and release the rest of excitation energy. In both processes, the released energy is transferred to lattice which causes heat transfer through the suspended sample.

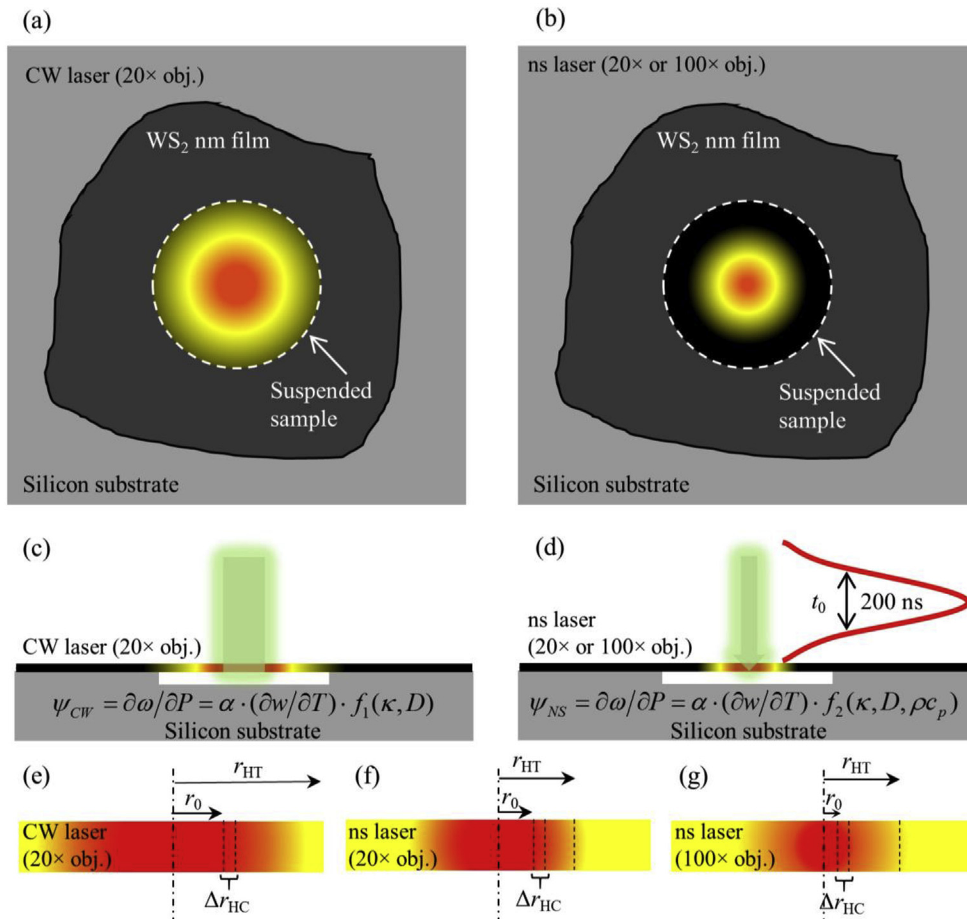

Fig. 2. (a) and (b) Exfoliated WS_2 thin films on Si substrate with a circular hole on it. Examined samples are irradiated using 532 nm lasers. (c) and (d) Using a continuous-wave laser (532 nm) and a nanosecond laser (532 nm), two different energy transport states are generated in both time and space (by using two objective lenses in ns case) domains. Raman shift power coefficient (ψ) carries information about the following parameters: laser absorption coefficient (α), Raman temperature coefficient ($\partial\omega/\partial T$), in-plane thermal conductivity (κ), hot carrier diffusivity (D), and ρc_p (in ns case). Using these three ψ values, we can measure κ and D. (e–g) Cross sectional view of heat diffusion length (r_{HT}), laser spot radius (r_0), and hot carrier diffusion length (Δr_{HC}) for three different cases. Under steady state heating, r_{HT} is equal to the radius of the suspended sample. Heat diffusion length during pulsed laser heating depends on laser pulse width and thermal diffusivity of the sample, therefore r_{HT} under two different ns cases are the same. Δr_{HC} is estimated using the *e-h* recombination time and hot carrier diffusivity and is the same for all three cases.

repetition rate and has two sub-states by using two different objective lenses (20 × and 100 ×). It is called near zero-transport state. By varying the local heating size, we can differentiate the effects of D and κ. This state is shown in Fig. 2(b) and (d). Again, like the steady state case, we obtain ψ for these sub-states as: $\psi_{ns20} = \partial\omega/\partial P$ and $\psi_{ns100} = \partial\omega/\partial P$. Both ψ values are a function of κ, D, ρc_p, α, and Raman temperature coefficient. The laser pulse width (200 ns) is much less than the interval between the two pulses (around 3 μs). Also, the pulse interval is much longer than the characteristic heat conduction time of the sample. So, after each heating period during the laser pulse, samples cool down to the initial temperature during the cooling period. Since the laser pulse width is not short enough to completely suppress heat diffusion, in these two cases, ψ is function of κ as well. Due to the moderate temperature rise in our measurement, we use a constant value for ρc_p which could be retrieved from literatures [43]. This assumption is assessed in Section 5.

In our Raman experiment, all the ψ values of WS_2 are Raman-intensity weighted average of the sample. Also, for the near zero-transport state, the temperature rise is time averaged over the pulse width. These details are all considered in our 3D (volumetric) numerical simulation. After doing the Raman experiments and obtaining ψ of all energy transport states, we define a new parameter (Θ) which is called normalized ψ value.

We define two Θ as: $\Theta_{20} = \psi_{ns20}/\psi_{CW}$ and $\Theta_{100} = \psi_{ns100}/\psi_{CW}$. By defining these two new parameters, we rule out the effects of laser absorption coefficient and Raman temperature coefficients. Measurement of these two coefficients is one of the main sources of uncertainty in previous Raman measurements. As a result, with known ρc_p value, Θ_{20} and Θ_{100} only depend on thin film's properties, such as κ and D. Finally, using a 3D heat conduction model that includes all the above-mentioned details, it is possible to determine κ and D of the WS_2 nm-thick films.

Generation and diffusion of heat and electrical carriers in the sample are governed by hot carrier diffusion equation and thermal diffusion equation. Hot carrier diffusion equation is used to determine the carrier concentration $\Delta N(r,t)$ (cm^{-3}) [44]:

$$\frac{\partial \Delta N}{\partial t} = D\nabla^2 \Delta N - \frac{\Delta N}{\tau} + \frac{\partial n_0}{\partial T}\frac{\Delta T}{\tau} + \Phi\alpha, \tag{1}$$

where τ (s), n_0 (m^{-3}), Φ (number of photons per m^{3}s), α (cm^{-1}), and ΔT (K) are e-h recombination time, equilibrium free carrier density at temperature T, incident photon flux, optical absorption coefficient of WS_2 nm-thick films, and temperature rise, respectively. The first and second terms on the right side represent the hot carrier diffusion and e-h recombination effects, respectively. The term $(\partial n_0/\partial T)(\Delta T/\tau)$ is related to hot carrier creation due to temperature rise and it is called thermal activation term, and the last term ($\Phi\alpha$) is the hot carrier photogeneration source. In this work, due to the low temperature rise and free-carrier density, the thermal activation term is negligible [45,46].

In order to investigate the thermal transport by phonons, the thermal diffusion equation is written as:

$$\rho c_p \frac{\partial \Delta T}{\partial t} = \kappa_{\parallel}\frac{1}{r}\frac{\partial}{\partial r}\left(r\frac{\partial \Delta T}{\partial r}\right) + \kappa_{\perp}\frac{\partial^2 \Delta T}{\partial z^2} + \alpha I\left(\frac{h\nu - E_g}{h\nu}\right) + \frac{E_g \Delta N}{\tau}, \tag{2}$$

where $\kappa_{\parallel}$ (W·m^{-1}·K^{-1}), $\kappa_{\perp}$ (W·m^{-1}·K^{-1}), $h\nu$ (2.33 eV), and E_g are in-plane thermal conductivity of WS_2, out-of-plane thermal conductivity of WS_2, photon energy of the laser beam, and WS_2 bandgap, respectively. To evaluate the thermal transport in the thickness direction (out-of-plane), we can estimate the effective heat diffusion length in this direction as: $L_{\perp} = \sqrt{\pi\alpha_{\perp}t_0}$, where $\alpha_{\perp}$ (m^2·s^{-1}) and t_0 (s) are thermal diffusivity in cross-plane direction and ns laser pulse width, respectively. Note that $\kappa_{\perp}$ of WS_2 is around 2 W m^{-1} K^{-1} which is much less than $\kappa_{\parallel}$ [47]. For the WS_2 nm-thick films under laser irradiation with $t_0 = 200$ ns, $L_{\perp}$ is in the order of 1 μm, which is much larger than the thickness of the measured samples. In fact, t_0 is long enough for the heat to be transferred all the way in the thickness direction. As a result, we can assume that the temperature distribution in the thickness direction (z-direction) is uniform. ($E_g\Delta N/\tau$) describes the energy coupling to phonons from the electron-hole recombination. Note that under steady state condition (CW laser), the term on the left side of both Eqs. (1) and (2) (time-dependent term) is 0. In following, we indicate the in-plane thermal conductivity by κ instead of $\kappa_{\parallel}$ for ease of discussion. In addition, I represents the laser intensity (W·m^{-2}), which is described as for ns laser:

$$I(r,z,t) = \frac{I_0}{\tau_L}\exp\left(-\frac{r^2}{r_0^2}\right)\exp\left[-\ln(2)\frac{t^2}{t_0^2}\right]\exp\left(-\frac{z}{\tau_L}\right), \tag{3}$$

where I_0 (W·m^{-2}), τ_L (m), r_0 (m), and t_0 (s) are peak laser intensity, laser absorption depth, laser spot radius, and half pulse width of the ns laser, respectively. τ_L is calculated as $\tau_L = \lambda/4\pi k_L$, where k_L is extinction coefficient and λ is laser wavelength. In this work, $\lambda = 532$ nm and using reference values for k_L, $\tau_L(WS_2) = 28.2$ nm [48–51]. In the following, it will be well proved that the value of τ_L has very little effect on κ and D measurement in our technique. It should be noted that under steady state laser heating, the third term in right side of Eq. (3) ($\exp[-\ln(2)t^2/t_0^2]$) is 1.

Heat and hot carrier diffusion lengths in the in-plane direction of suspended sample are estimated and shown in Fig. 2(e–g). In addition, laser spot radius (r_0) is also indicated to discuss the physics. Under CW laser heating, since laser heats the sample continuously, heat transfers all the way until the boundary of the sample. While under pulsed laser heating, heat diffusion length can be estimated as: $r_{HT} = 2\sqrt{\alpha t_0}$, and here α is thermal diffusivity [52]. As indicated in this formula, heat diffusion length under the pulsed laser irradiation does not depend on the objective lens and it is similar for both 20 × and 100 × objectives. For all the three cases, hot carrier diffusion length (Δr_{HC}) is calculated as: $\Delta r_{HC} = \sqrt{\tau D}$ [53]. For WS_2 films, τ and D are in the order of 0.1 ns and 1 cm^2 s^{-1}, so Δr_{HC} is in order of 0.1 μm.

Note that heat transfer by air convection has negligible effect on our measurement. To evaluate it, the thermal resistance caused by air convection on both sides of the suspended sample (R_h) and thermal resistance caused by heat conduction through the in-plane direction (R_c) for a sample with 107 nm thickness are estimated as below as $R_h = 1/(hA) = 1/(2\pi r_0^2 h)$ and $R_c = \ln(r_1/r_0)/(2\pi l\kappa)$. Here r_0, r_1, h, l, and κ are the radius of laser spot, radius of suspended area, convection heat transfer coefficient of air, sample thickness, and in-plane thermal conductivity of WS_2, respectively. Here, we estimate the convection heat transfer coefficient of air as 20 W/m^2·K, which is a high-end one for natural convection. Using a sample thermal conductivity of 39 W/mK, radius of 5 μm, and laser spot radius of 1.8 μm, R_h is calculated as 2.46×10^9 K/W and R_c as 3.92×10^4 K/W. It is clear that the thermal resistance caused by air convection is much higher than the one caused by in-plane heat conduction through laser heating. For samples of a few nm thickness, the ratio of R_h/R_c is still in the order of 100. Therefore, it is reasonable to neglect the effects of free convection heat transfer. For radiation effect, the equivalent h is in the order of 5 W/m^{2}K, making the radiation thermal resistance orders of magnitude higher than that of in-plane heat conduction.

3. Experimental details

Fig. 3(a) shows the Raman setup of the experiment. This system consists of a CW laser (532 nm) (Xcelsior-532-150-CDRH Spectra-Physic) and a nano-second (ns) pulsed laser (532 nm) (DCL AIO Laser, Photonics Industries, International, Inc.) as energy sources and a microscope (Olympus BX53) and Raman spectrometer (Voyage, B&W Tek, Inc.). In order to adjust the laser power, a motorized neutral density (ND) filter (CONEX-NSR, Newport Corporation) is used. All these components are controlled by a LabVIEW-based software, which ensures highest accuracy of the experiment as well as reducing the experiment time. More details about this Raman system could be found in our previous works [27,30,54]. The atomic structure and Raman spectrum of WS_2 is shown in Fig. 3(b) and (c). The W atoms are in middle of each layer and sandwiched between S atoms. The Raman spectrum has two vibrational modes of WS_2 (E^1_{2g} and A_{1g}) under irradiation of 532 nm wavelength laser. The A_{1g} mode (419 cm^{-1}) is associated with the out-of-plane vibration mode of sulfur atoms in opposite directions. The other main Raman peak is E^1_{2g} mode (348 cm^{-1}) at lower wavenumbers than A_{1g} mode and is associated with the in-plane opposite vibration of two sulfur atoms with respect to the tungsten atom [55]. Here, since the E^1_{2g} peak is stronger and therefore more reliable for data fitting, we use it to perform our measurement.

Fig. 3(d) shows energy distribution contours under 20 × (for both CW and ns cases) and 100 × (only ns case) objective lenses taken by a CCD (Olympus DP-26, Olympus Optical Co., Ltd.) camera. These images are analyzed by a Gaussian fitting method to determine the laser spot radius. For the 13 nm sample, the Gaussian beam spot size r_0 (at e^{-1} peak value) is measured as 1.667, 1.138, and 0.311 μm, under 20 × (CW laser), 20 × (ns laser), and 100 × (ns laser) objective lenses, respectively. Laser spot radii of all measurements are shown in Table 1.

4. Samples preparation and characterization

In this work, four suspended WS_2 samples are prepared on Si substrate with a 10 μm diameter hole on it using the mechanical exfoliation method from a bulk WS_2 crystal. Due to the weak van der Waals force between WS_2 layers, it is easy to exfoliate thin layers. First, layers of WS_2 are peeled off from bulk material using the scotch tape and then are transferred to gel films. Finally, we transfer the thin layer of WS_2 to silicon substrate with a hole in the middle. Using this method, we can make samples with pristine, clean, and high-quality structure [56]. More details about this method of fabrication can be found in our previous works [30]. Fig. 4(a1-d1) shows the AFM images of these four samples. Their thicknesses are 13, 49, 60, and 107 nm. The supported area near the suspended area is used to perform the AFM imaging. The red line on the boundary of the WS_2 and Si corresponds to the height profile of the sample, which is shown in Fig. 4(a2-d2). Fig. 4(a3-d3) shows the roughness profile of each sample and Δl_{max} represents the largest surface height variation along a straight line on the sample surface. Δl_{max} is relatively small in comparison with the sample thickness. Especially for thicker samples, it is less than 5% of the measured sample thickness. Wrinkles or ripples in the samples are the main factors that cause thickness variation. Below, the 13 nm sample is used to explain the technique and results.

5. κ and D measurement

Fig. 5(a–c) show the 3D contour map of WS_2 Raman peaks (A_{1g} and E^1_{2g}) for the 13 nm sample. Under all different lasers and objective lenses, the E^1_{2g} peak is stronger than A_{1g}. For both peaks, the Raman intensity increases with the increased laser power. Laser power ranges of all three cases for four samples are included in Table 2. The Raman intensity has almost a linear relationship with laser power and discrepancy in it could be caused by uncertainties in Gaussian fitting of Raman spectrums or the effect of laser heating. For higher laser power, as the laser power and consequently local temperature increase, the Raman excitation efficiency will decrease [57,58]. In addition, as shown in this figure, for ns case under 100 × objective with a lower laser power, the Raman intensity is higher than ns with 20 × objective lens. 2D contour maps of Raman peak intensity are represented in Fig. 5(d–f). It indicates the redshift of Raman peaks for all cases with increased laser power.

Fig. 6(a–c) show the Raman spectrum for different laser powers

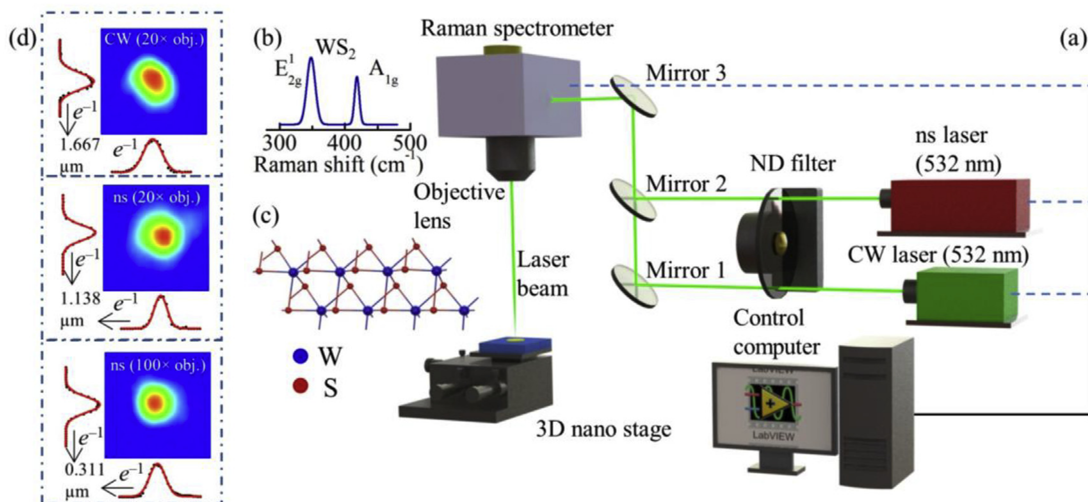

Fig. 3. Schematic of the Raman system. (a) WS_2 thin films are illuminated by a CW and a ns laser separately. Laser power is adjusted by a ND-filter that is controlled by a LabVIEW-based program, and Raman spectrum is collected by Raman spectrometer. (b) Raman spectrum of WS_2 sample excited by 532 nm lasers. Both E^1_{2g} and A_{1g} peaks are observed. Since the E^1_{2g} peak is stronger, it is used in our data processing. (c) Atomic structure of WS_2. Blue balls represent tungsten (W) atoms and red balls indicate sulfur (S) atoms. (d) The spatial energy distribution of the laser beam under three different energy states for a 13 nm-thick sample. The black points are laser beam intensity data collected by CCD camera and red lines indicate the Gaussian data fitting. Using this energy distribution and data fitting, laser spot's radius is measured. (For interpretation of the references to colour in this figure legend, the reader is referred to the Web version of this article.)

Table 1
Summary of laser spot size under three different heating states.

Sample thickness (nm)	CW laser spot radius under 20 × objective lens (μm)	ns laser spot radius under 20 × objective lens (μm)	ns laser spot radius under 100 × objective lens (μm)
13	1.667	1.138	0.311
49	1.599	1.060	0.318
60	1.648	1.031	0.330
107	1.797	1.270	0.344

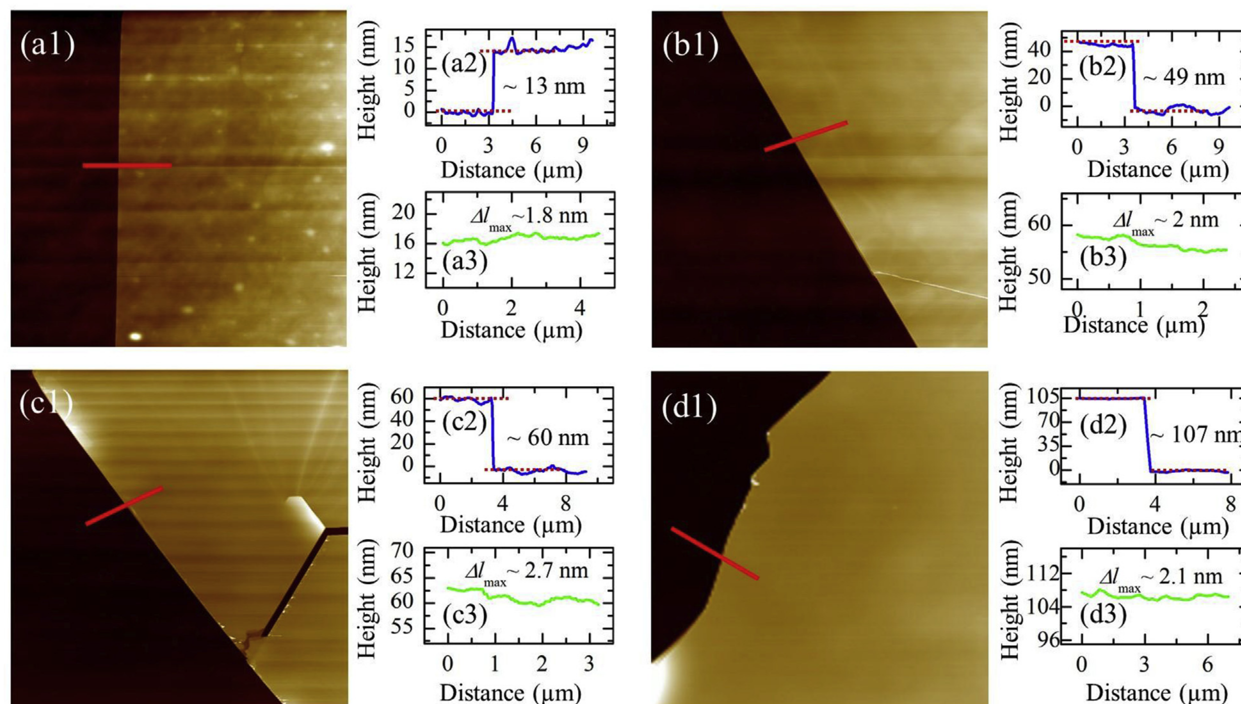

Fig. 4. AFM imaging of the four WS_2 samples. AFM test is conducted on supported area of each sample to prevent damage of suspended area. (a1-d1) AFM images of all samples. (a2-d2) Thickness profiles of the samples which correlate with the solid red lines. (a3-d3) Thickness profiles on surface area that indicates the sample roughness. (For interpretation of the references to colour in this figure legend, the reader is referred to the Web version of this article.)

under all thermal transport states. It also indicates the redshift of Raman peaks by increased laser power. It shows that in low laser power range, Raman shift and laser power are linearly correlated. Note that this laser power is just before the laser irradiates the sample and it should maintain as low as possible to prevent photon absorption saturation [59,60]. Using this linear relationship, we obtain the ψ values of the 13 nm-thick sample under three states as: $-(0.78\pm0.01)$ $cm^{-1}\,mW^{-1}$, $-(3.78\pm0.06)$ $cm^{-1}\,mW^{-1}$, and $-(11.2\pm0.1)$ $cm^{-1}\,mW^{-1}$ under CW under 20 ×, ns under 20 ×, and ns under 100 × objectives, respectively. Table 3 includes the ψ values of all four samples. Generally, ψ of each state decreases with the increased sample thickness. In fact, ψ represents the temperature rise under unit laser power irradiation. Lower ψ values mean lower temperature rise which means thicker samples could better dissipate heat. In fact, the temperature rise under unit laser power (ΔT) is directly proportional to absorbed laser energy (ΔE) and inversely proportional to κ and thickness (t) as: $\Delta T \propto \Delta E/\kappa t$. Note that the absorbed laser energy (ΔE) normally increases with increased film thickness, but the increasing ratio is less than t. Thicker samples has a larger cross-section and can conduct heat better than thinner ones (proportional to t). Consequently, the temperature rise will be lower than that of thinner samples. Another factor that affects ΔT is κ. As will be mentioned in the following discussion, κ increases with increased sample thickness. This provides another contributing factor for the observed decrease of ψ with increased sample thickness. Additionally, for each sample, the ψ value of ns case under 100 × objective lens is more than the ψ of ns under 20 × objective lens. Objective lenses with higher magnification (or smaller r_0) intensify the laser power per unit area which leads to increase in local temperature rise.

In order to determine the temperature rise and consequently the in-plane thermal conductivity (κ) and hot carrier diffusion coefficient (D) of thin films, we conduct a 3D numerical modeling based on the finite volume method. In this work, the ballistic effect on thermal transport is not of great importance, because the phonon mean free path (MFP) of WS_2 samples is far less than the laser spot sizes. In fact, phonon MFP of WS_2 is around 15 nm which is smaller than all laser spot sizes (Table 1) [26,61,62]. Here, as mentioned earlier, we take the 13 nm-thick sample as an example to discuss the simulation and experimental results. Using our 3D numerical simulation, we can calculate Θ_{20} and Θ_{100} in the (κ, D) space. By doing so, any effect of laser absorption coefficient and Raman temperature coefficient is eliminated. Table 3 includes the Θ values of all four samples. Θ_{20} and Θ_{100} increase with increased sample thickness. As discussed earlier, for a specific sample, under ns case thermal transport is mostly restricted to laser spot area [Fig. 2(f) and (g)], while under CW state it transfers until the boundaries of suspended sample [Fig. 2(e)]. This means that under

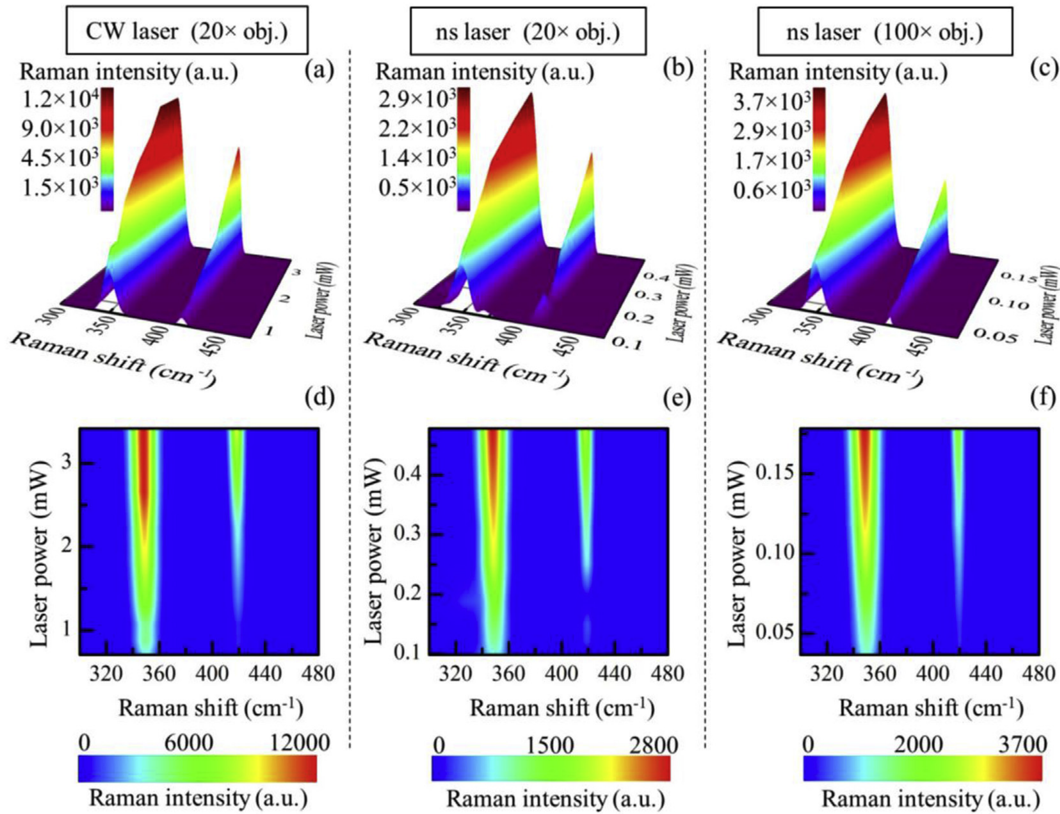

Fig. 5. Contour maps of the 13 nm-thick WS_2 sample. (a–c) Raman intensity variation under three different cases with respect to laser power represented by 3D contour maps. (d–f) The variation of Raman shift of both WS_2 peaks against laser power for all three cases.

Table 2
CW and ns laser power ranges of all three heating states for four WS_2 samples.

Sample thickness (nm)	CW laser power range under 20 × objective lens (mW)	ns laser power range under 20 × objective lens (mW)	ns laser power range under 100 × objective lens (mW)
13	0.705–3.418	0.097–0.478	0.037–0.178
49	0.578–2.801	0.099–0.478	0.046–0.224
60	0.665–3.222	0.124–0.602	0.037–0.178
107	1.480–7.172	0.221–1.070	0.092–0.448

CW case, the effect of thermal conductivity on thermal transport is more significant than under ns cases. Therefore, Θ_{20} and Θ_{100} are approximately inversely proportional to in-plane thermal conductivity. The laser absorption depth is another parameter that should be considered in the simulation. Here, we take $\tau_L = 28.2$ nm, while as we discussed in Section 6.3, the value of τ_L has negligible effect in the determined values of κ and D.

Fig. 7(a) and (b) show the calculated Θ values and solid lines indicate the experimental values of Θ. In both Raman experiment and numerical calculations, the measured Θ of WS_2 samples are Raman-intensity weighted average of the suspended film. Raman-intensity weighted average temperature under CW is calculated as: $\overline{T}_{CW} = \int_0^V Ie^{-z/\tau_L}Tdv / \int_0^V Ie^{-z/\tau_L}dv$, where I is laser intensity, T is temperature of each point, V is the volume of sample, and term e^{-z/τ_L} is Raman signal attenuation when the signal leaves the scattering location. Additionally, for the ns case, the temperature rise is averaged in time domain as well as space domain. Therefore, under ns cases, Raman-intensity weighted average temperature rise is calculated as: $\overline{T}_{ns} = \int_0^t \int_0^V Ie^{-z/\tau_L}Tdvdt / \int_0^t \int_0^V Ie^{-z/\tau_L}dvdt$. It should be noted that local Raman intensity is proportional to the local laser. As shown in Fig. 7(a), lower D implies higher Θ values. This effect is more obvious in Fig. 7(b), due to the smaller laser spot size of the ns case. The lower is D, the more heating area will be restricted to the laser spot area, and it results in a higher local temperature rise of the sample. To further illustrate this effect, calculated temperature rise under three different cases are plotted in Fig. 7(d). Here, we can see again that as laser spot size becomes smaller, effects of D on temperature rise become more prominent. In fact, when the hot carrier diffusion length (Δr_{HC}) is more than (or comparable with) laser spot radius (r_0), hot carriers could diffuse out of the heating area easier. In addition, Fig. 7(d) indicates that the temperature rise of the sample is higher when thermal conductivity is lower. Note that lower κ values will result in lower Θ values. It comes from the point that temperature rise is more sensitive to κ under CW case than ns case. This effect is clearly indicated in temperature rise contour in Fig. 7(d). When κ decreases from 25 to 10 W m^{-1} K^{-1}, the temperature rise of the sample under CW increases more than 300%, while under ns case it increases by less than 100%. This effect is also indicated in inset of Fig. 7 (b). In this plot, the temperature rise under three heating states are

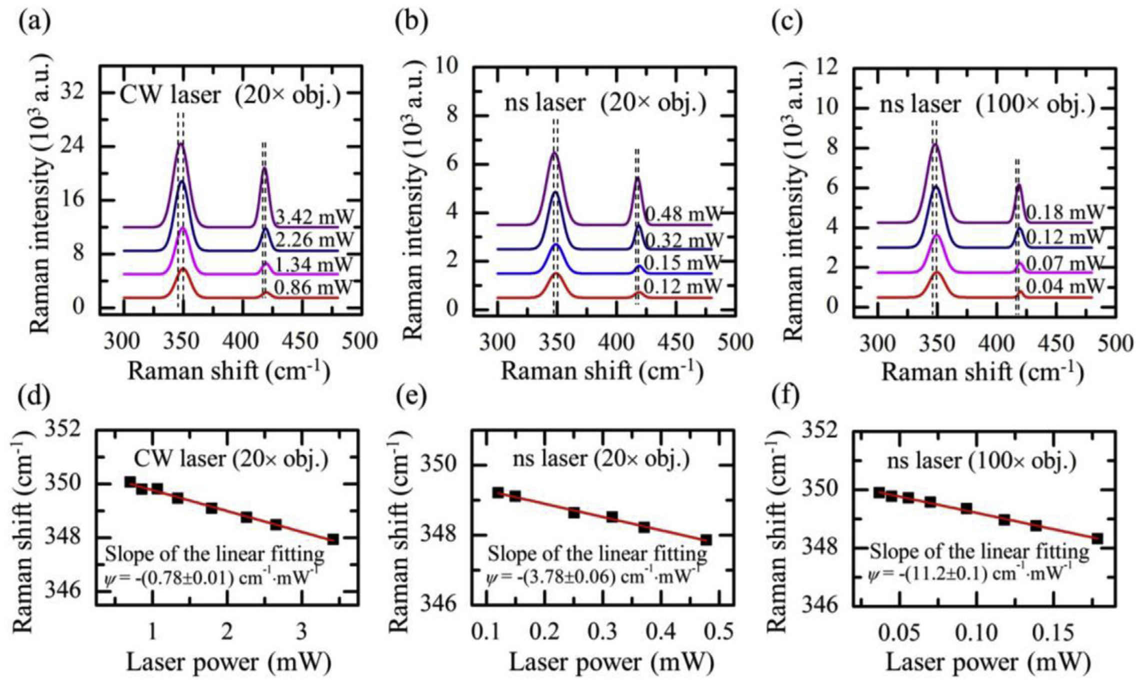

Fig. 6. (a–c) Four representative room temperature Raman spectra under three thermal transport states. Black dashed lines indicate the redshift of Raman peaks with increased laser power. (d–f) Linear dependency of Raman shift on laser power, and ψ of 13 nm-thick sample in low laser power range.

Table 3
Summary of the E^1_{2g} mode ψ values under three heating states for all four samples.

Sample thickness (nm)	E^1_{2g}, CW (cm^{-1} mW^{-1})	E^1_{2g}, ns, 20 × (cm^{-1} mW^{-1})	E^1_{2g}, ns, 100 × (cm^{-1} mW^{-1})	Θ_{20}	Θ_{100}
13	−(0.78 ± 0.01)	−(3.78 ± 0.06)	−(11.2 ± 0.1)	4.85 ± 0.10	14.4 ± 0.2
49	−(0.42 ± 0.01)	−(2.66 ± 0.05)	−(6.40 ± 0.11)	6.34 ± 0.20	15.2 ± 1.5
60	−(0.37 ± 0.01)	−(2.53 ± 0.05)	−(5.88 ± 0.16)	6.88 ± 0.17	15.9 ± 0.5
107	−(0.21 ± 0.01)	−(1.63 ± 0.03)	−(3.95 ± 0.04)	7.69 ± 0.28	18.7 ± 0.6

calculated against several D values while κ is set constant. It confirms that under smaller heating spot sizes D has more contribution to temperature rise variation.

As discussed earlier, each experimental Θ value could take several κ and D values, as shown by solid lines in Fig. 7(a) and (b). We use these black (Θ_{20}) and red (Θ_{100}) solid lines to plot them in a (κ, D) space to find their cross-point. Fig. 7(c) represents this cross-point. By doing so, κ and D are determined as 15.1 W m^{-1} K^{-1} and 1.78 cm^2 s^{-1}, respectively. We use the normalized probability distribution function (Ω) to calculate the uncertainty of κ and D [27]. This function is defined as: $\Omega = \exp[-(x-\bar{x})^2/2\sigma^2]$, where x is the variable, and $\bar{x}$ and σ are its average and standard deviation, respectively. Ω is plotted as contour in Fig. 7(c). In the (κ, D) space, we define $\Omega_{(\kappa,D)} = \Omega_{\Theta_{20}} \cdot \Omega_{\Theta_{100}}$. Finally, by setting $\Omega_{(\kappa,D)} = 0.6065$ corresponding to σ confidence, the uncertainty of κ and D are obtained. Final values of κ and D for the 13 nm-thick sample are $15.1^{+0.3}_{-0.4}$ W·m^{-1} K^{-1} and $1.78^{+0.5}_{-0.6}$ cm^2·s^{-1}, respectively.

As discussed in the physical model section, due to the Coulomb attraction, electron (e) and holes (h) move together during the diffusion process. Therefore, the determined D is the ambipolar diffusion coefficient, $D = 2D_eD_h/(D_e + D_h)$, where $D_{h(e)}$ is unipolar diffusion coefficient of holes (or electrons) [63]. In our optical study, the effective mass of electrons and holes are comparable, and equal number of them are generated under laser heating. As a result, it is physically reasonable to assume that D_e and D_h are equal and approximate D as the unipolar diffusion coefficient of both electrons and holes. Additionally, in order to determine the carrier mobility μ, we use the Einstein relation as $\mu = Dq/k_BT$, where k_B, q, and T are Boltzmann constant, charge of each carrier, and temperature, respectively [64]. Here, T takes 298 K. For the 13 nm-thick WS_2 nanosheet, the measured μ is 69.8 cm^2 V^{-1} s^{-1}. Generally, for all the multilayer samples, it is in order of 100 cm^2 V^{-1} s^{-1}. This result is in good agreement with literature values of 234 cm^2 V^{-1} s^{-1} reported by Liu et al. [65], 50 cm^2 V^{-1} s^{-1} by Ovchinnikov et al. [66], and 20 cm^2 V^{-1} s^{-1} [67,68]. Results of all measured properties are included in Table 4.

To find the effect of sample thickness on in-plane thermal conductivity (κ), measured κ values in this work or other works are summarized in Fig. 8(a) against their thickness [33,69]. Considering our result and other works, a nonmonotonic distribution of κ versus thickness can be observed. For monolayered or few-layered samples which are indicated to the left side of the gray dashed line, the thermal conductivity decreases with increased thickness. This trend is attributed to higher anharmonicity of thicker films in this range [70]. In other words, phonon scattering in monolayered films is mostly controlled by boundary scattering, and effects of Umklapp scattering is less significant. Umklapp scattering becomes more considerable as the thickness increases. However, this trend reverses on the right side of the gray dashed line for thicker samples. In this range, thermal conductivity has a direct relationship with thickness. This effect is due to the reduced effect of surface scattering in thicker suspended films. Effects of surface scattering on thermal conductivity can be analyzed by the Landauer approach using the phonon Boltzmann transportation equation and Fuchs-

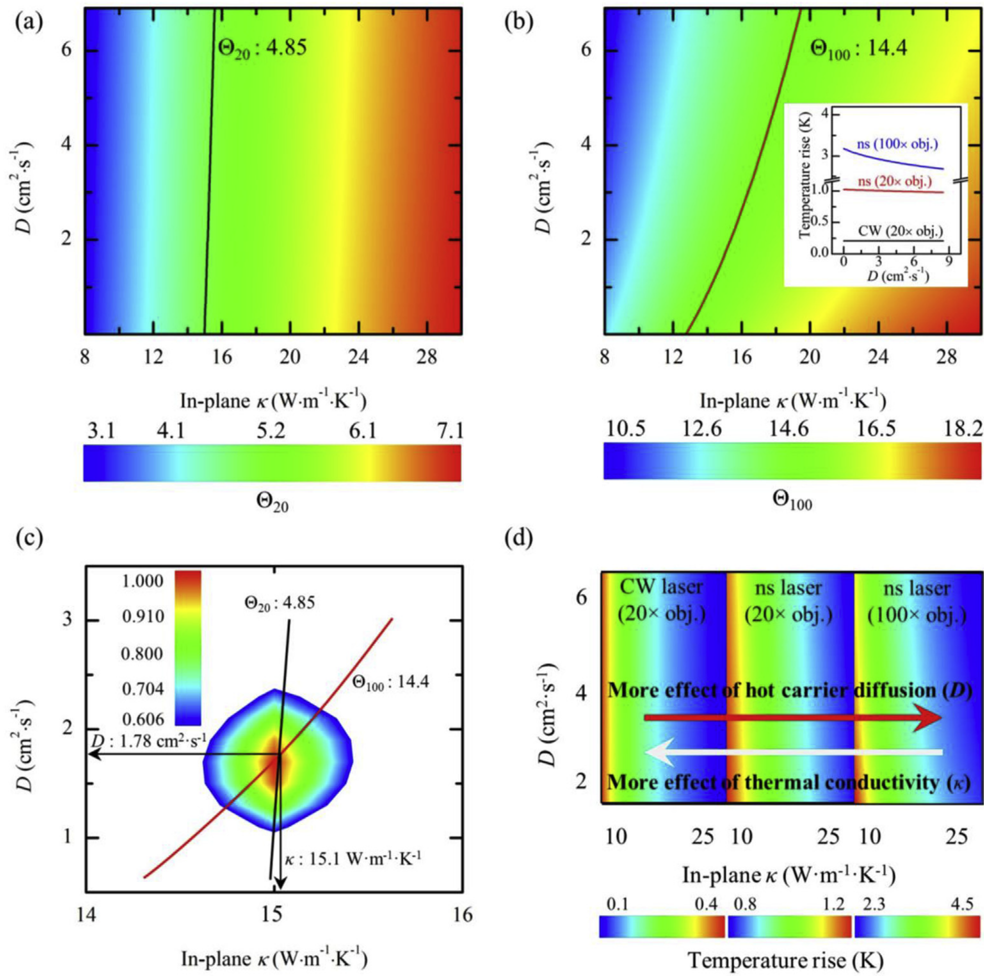

Fig. 7. (a) and (b) Θ (normalized Raman shift power coefficient) for different κ and D values obtained by 3D numerical modeling of the 13 nm-thick sample under (a) 20 × and (b) 100 × objectives. Solid lines represent Θ obtained from the Raman experiment. The inset in figure (b) shows the temperature rise under each of the three cases against several D values. Temperature rise is more sensitive to D for smaller laser spot size. (c) Measured κ and D and calculated uncertainty contour using the normalized probability distribution function (Ω). (d) Calculated Raman-intensity weighted average temperature rise using our 3D modeling for three cases to show the sensitivity of temperature rise to κ and D.

Table 4
Summary of the determined in-plane thermal conductivity (κ), hot carrier diffusion coefficient (D), corresponding hot carrier diffusion length (Δr_{HC}), and carrier mobility (μ).

Sample thickness (nm)	κ ($W \cdot m^{-1} \cdot K^{-1}$)	D ($cm^2 \cdot s^{-1}$)	Δr_{HC} (μm)	μ ($cm^2 \cdot V^{-1} \cdot s^{-1}$)
13	$15.1^{+0.3}_{-0.4}$	$1.78^{+0.5}_{-0.6}$	$0.14^{+0.02}_{-0.02}$	$69.8^{+20.8}_{-23.1}$
49	$22.8^{+1.3}_{-1.3}$	$2.7^{+4.8}_{-2.6}$	$0.17^{+0.15}_{-0.08}$	$106.2^{+187.8}_{-99.9}$
60	$23.8^{+1.1}_{-1.1}$	$1.43^{+1.5}_{-1.2}$	$0.13^{+0.07}_{-0.05}$	$56.1^{+60.4}_{-45.1}$
107	$38.8^{+2.6}_{-2.4}$	$7.05^{+4.3}_{-3.1}$	$0.28^{+0.08}_{-0.06}$	$276.4^{+166.6}_{-121.9}$

Sondheimer approach which are illustrated in details in our previous works for MoS_2 and $MoSe_2$ nm-thick films [29,30,54].

Fig. 8(b) represents the hot carrier diffusion coefficient (D) against thickness for WS_2 and MoS_2 samples. As we mentioned earlier, very rare works are done on investigating the hot carriers' behavior of WS_2, so MoS_2 data of our previous work is included in this plot as well [28]. Additionally, results of work by He et al. for both monolayered and bulk WS_2 samples are included in Fig. 8(b) [26]. Considering our four samples, hot carrier diffusion coefficient (D) remains almost constant for first three samples and increases a little bit for the thickest one. Our result for multilayered films is in good agreement with previous data of bulk WS_2 [26]. Similar trend is observed for carrier mobility (μ) (Table 4). For suspended samples with more than few-layers, phonon scattering is mostly controlled by temperature and structure of the sample. In our experiment, since temperature of all samples are almost equal, we can expect that lattice scattering due to the temperature rise remains constant for all samples. However, D of 107 nm sample is much higher than that of the other three samples. Any discrepancy between these results could be caused by different structure of WS_2 layers and Raman experiment uncertainties. In fact, the samples made by mechanical exfoliation method could have some differences in their structures. These structural differences are in form of defects and different surface conditions. Additionally, uncertainty of D measurement could be optimized as will be mentioned in following sections.

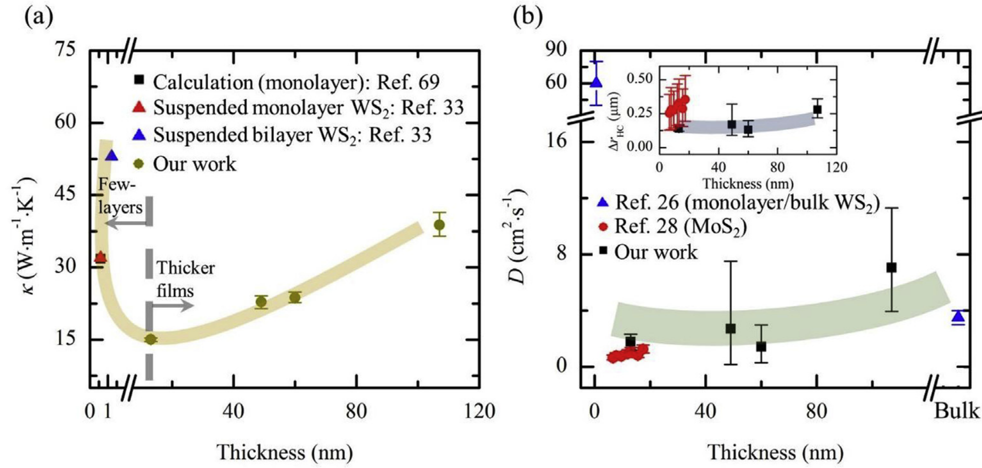

Fig. 8. (a) and (b) Summary of in-plane κ and D in this work and previous works, respectively. Inset of (b) shows the determined hot carrier diffusion length in this work and one of our previous works.

However, D and Δr_{HC} of MoS_2 thin samples experience an increasing trend against thickness. This phenomenon was attributed to several factors. First, it may be caused by the effect of Coulomb scattering from charge impurities for thicker samples. In fact, the effect of charge impurities and the substrate could be mitigated relatively for thicker samples which consequently leads to higher mobility [71–73]. Additionally, this effect may be caused by weaker electron-phonon interaction of thicker films [71]. Uncertainties of determined κ and D are also plotted in Fig. 8(a) and (b). This uncertainty is due to the ψ fitting procedure, and other parameters, such as laser spot location. Detailed discussion regarding these factors are given in following sections. Additionally, as indicated in Table 4 and Fig. 8, D has a higher uncertainty than κ. As shown in Fig. 7(d), as local heating size decreases, effects of hot carrier diffusion (D) becomes more prominent and consequently will lead to a lower uncertainty of measured D values. In fact, the hot carrier can be very dominant in ultra-small heating states and is negligible in very large size heating states. As a result, if we perform the Raman experiment under an extreme small size heating state, the uncertainty of determined D could be significantly reduced.

In our technique, the measured D value is dependent on the recombination time of hot carriers (τ). To further illustrate this effect, we define $\gamma = \Delta N/\tau$ as normalized hot carrier concentration, and rewrite Equations (1) and (2) as:

$$\tau\frac{\partial\gamma}{\partial t} = \Delta r_{HC}^2\nabla^2\gamma - \gamma + \Phi\alpha \tag{4}$$

$$\rho c_p\frac{\partial\Delta T}{\partial t} = \kappa\frac{1}{r}\frac{\partial}{\partial r}\left(r\frac{\partial\Delta T}{\partial r}\right) + \alpha I\left(\frac{h\nu - E_g}{h\nu}\right) + E_g\gamma \tag{5}$$

Note that thermal activation and thermal transport in cross-plane direction terms are neglected in these two equations, as explained before. Also, since the laser pulse width is much longer than the hot carrier lifetime, the term $\tau\partial\gamma/\partial t$ in equation (4) becomes negligible. By solving equations (4) and (5) we determine hot carrier diffusion length (Δr_{HC}) without knowing the hot carriers' properties. And finally, D could be calculated using the carrier lifetime (τ) as $D = \Delta r_{HC}^2/\tau$. In this work, τ takes 0.11 ns [26]. Table 4 and inset of Fig. 8(b) shows the determined hot carrier diffusion length (Δr_{HC}) against sample thickness. Δr_{HC} of all four WS_2 samples are in order of 200 nm Δr_{HC} of WS_2 is less than that of MoS_2 measured by Yuan et al. [28] which may be attributed to lower *e-h* recombination time of the WS_2.

As mentioned earlier, ρc_p and κ are taken constant in this work. Here we use the 13 nm-thick sample to justify this assumption. As shown in Fig. 6, redshift ($\Delta\omega$) of the CW state is 1.04 cm^{-1}. Using this value and Raman temperature coefficient (α) of 0.014 cm^{-1} K^{-1} [33], we can calculate the temperature rise of the sample under laser spot as $\overline{T}_{es} = \Delta w/\alpha = 74$ K. To check the amount of thermophysical properties' changes, we need to determine the average temperature rise of entire suspended sample. It is calculated as: $\overline{T}_{tf} = \int_0^R T(r)rdr/\int_0^R rdr$, where R is the radius of suspended film and $T(r)$ is temperature of each point in calculation domain. Using $\overline{T}_{es}$, $\overline{T}_{tf}$, and $\overline{T}_{CW}$ (or $\overline{T}_{ns}$) that introduced earlier, the temperature rise of entire sample under laser irradiation is calculate as: $\overline{T}_{ef} = \overline{T}_{tf}\times(\overline{T}_{es}/\overline{T}_{CW})$. $\overline{T}_{ef}$ for CW, ns under 20 × objective, and ns under 100 × objective states are calculated as 34.1 K, 27.2 K, and 11.1 K, respectively. O'Hare et al. [43] reported c_p of WS_2 at different temperatures. When temperature change of the sample is less than 40 K, c_p (and ρc_p) change is less than 3%. Therefore, it is physically reasonable to assume that ρc_p remains constant during our Raman experiment.

6. Discussion

6.1. State design for D and κ measurement

As we discussed earlier, the size of heating state (laser spot size) can affect the uncertainty of measured D and κ. Theoretically, it is possible to determine D and κ using other heating states, however the accuracy of measurement will be reduced. Another possible way to design the heating states is to conduct the Raman experiment with steady state laser under 100 × objective lens, instead of the ns laser under 100 × objective lens. As a result, we can determine D and κ using these three states: CW under 20 × objective, CW under 100 × objective, and ns under 20 × objective. Using these three states, we again obtain two normalized Θ values as: $\Theta_{20/20} = \psi_{ns20}/\psi_{CW20}$, and $\Theta_{20/100} = \psi_{ns20}/\psi_{CW100}$. First state ($\Theta_{20/20}$) is similar to Θ_{20} introduced in section 2. As shown in Fig. 7(a), using the first state ($\Theta_{20/20}$ or Θ_{20}), we can determine κ with a very small uncertainty, since Θ is almost only sensitive to κ and not D. Therefore, $\Theta_{20/100}$ is very critical to minimize the uncertainty of D. Fig. 9(a) shows the calculated temperature rise of the 13 nm-thick sample under steady state heating with 100 × objective lens. Also,

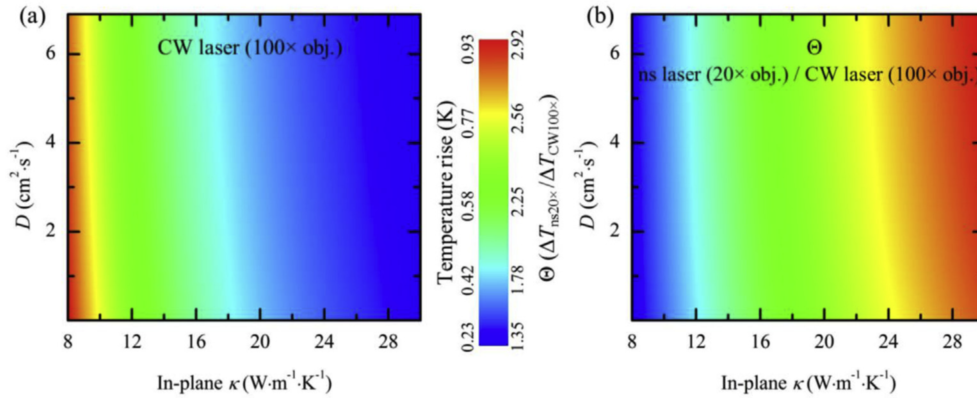

Fig. 9. Alternative state design by substituting the ns state under 100 × objective with CW state with similar heating size. (a) Temperature rise of the 13 nm-thick sample under this new state. In comparison to CW state under 20 × objective [Fig. 7(d)], the temperature rise under this state is more sensitive to D as could be seen by comparing their contours. Under CW (20 × obj.), this contour shows that the hot carrier diffusion coefficient has negligible contribution on temperature rise variation. On the other side, temperature rise variation in (κ, D) domain under ns (100 × obj.) state is more sensitive to D values [Fig. 7(d)] than this new state. (b) Θ of this new designed state. In comparison to our first and original design using ns state (100 × obj.) which is shown in Fig. 7(b), the Θ contour is less sensitive to D that leads to larger uncertainty of determined hot carrier diffusion coefficient.

the temperature rise of the sample using ns laser under 100 × objective was plotted in Fig. 7(d). By comparing these two contours, we find that state CW under 100 × objective is less sensitive to D than ns state under similar objective. To explore it more, calculated normalized Θ using this state ($\Theta_{20/100}$) is plotted in Fig. 9(b). Again, while comparing Figs. 9(b) and Figure 7(b), we can clearly conclude that the accuracy of the experiment will be reduced by using steady state (CW) under 100 × objective instead of the ns state with similar objective lens.

6.2. Effect of pulsed laser pulse width on measurement accuracy

Another parameter that can affect the measurement accuracy is pulse width of the ns laser. As mentioned earlier, heat diffusion length (r_{HT}) under ns laser heating depends on thermal properties of sample (α) and the laser pulse width (t_0). As laser pulse width (t_0) decreases, the heat diffusion length decreases, too. Additionally, the hot carrier effect on thermal transport can be evaluated by comparing the hot carrier diffusion length (Δr_{HC}) with heat diffusion length (r_{HT}). In ns pulsed Raman experiment, if the pulse width is shorter, but still longer than the hot carrier recombination time, then the heat diffusion length will be shorter during pulsed heating, so the hot carrier effect can be more prominent. For instance, while all the parameters, such as D, α, and τ, are fixed and we decrease the laser pulse width from 200 ns to 50 ns, the ratio of heat diffusion length to hot carrier diffusion length ($r_{HT}/\Delta r_{HC}$) will be decreased by 50%. This shows the importance of t_0 and how it affects the precision of our technique. To show the effect of t_0 on measurement accuracy, we changed the pulse width from 1 ns to 200 ns and calculated the uncertainty of determined κ and D under several cases with the fixed κ and D values as 15.1 W m^{-1} K^{-1} and 1.78 cm^2 s^{-1}, respectively. Results of this analysis are shown in Fig. 10(a). Generally, the uncertainty of measured κ and D improves with decreased t_0. This effect is more prominent for determining D.

6.3. Effect of laser absorption level

As mentioned earlier, unlike steady state Raman measurements that uses laser absorption coefficient to determine thermal conductivity (κ), our measurement although uses the optical absorption depth in data processing, this data has almost no effect in final results. For instance, Chen et al. reported that 0.2% uncertainty in optical absorption of ~3% causes ±7% uncertainty in determined laser power (Q), which is the most significant source of error while measuring κ of suspended graphene [74,75]. The temperature rise of sample under laser irradiation depends on downward irradiation of the laser as well as the laser reflected back from the bottom. On the other side, regardless of which direction laser propagates through the sample, temperature rise is uniform in the thickness direction and is proportional to laser power. Therefore, the amount of laser reflected back does not affect κ and D determination and cancels out during our ratio calculation:

$$\frac{\Delta T_{t,ns}}{\Delta T_{t,CW}} = \frac{\Delta T_{r,ns}}{\Delta T_{r,CW}} = \frac{\Delta T_{t,ns} + \Delta T_{r,ns}}{\Delta T_{t,CW} + \Delta T_{r,CW}}, \quad (6)$$

where $\Delta T_{t,ns}$ and $\Delta T_{t,CW}$ are temperature rise of the sample generated by the laser coming down under ns (either 20 × or 100 × objective lens) and CW lasers, respectively. And $\Delta T_{r,ns}$ and $\Delta T_{r,CW}$ are temperature rise of the sample generated by the laser reflecting back under ns (either 20 × or 100 × objective lens) and CW cases, respectively.

To show the effect of laser absorption depth (τ_L) in our measurement, we calculated κ and D of 13 nm-thick sample using several τ_L values. In fact, by doing several numerical calculations using different τ_L values, we can obtain κ and D of this sample using the Θ obtained from the experiment (Table 3). Fig. 10(b) shows the determined κ (left vertical axis) and D (right vertical axis) for a wide range of laser absorption depth from 5 to 30 nm. Note that actual τ_L of WS_2 thin films is 28.2 nm, as mentioned in section 2. Also, the uncertainty of measured κ and D is calculated. As shown in this plot, κ remains almost unchanged against various τ_L values. Additionally, determined D values using τ_L close to actual value of τ_L (28.2 nm) are almost similar, and as τ_L becomes smaller, the effect of τ_L becomes more significant and D deviates more from the actual calculated D. Uncertainties of κ and D for each τ_L is also calculated and shown in this figure. As indicated in this figure, these uncertainties do not change with τ_L.

To further clarify the effect of τ_L on κ and D determination, percentage deviations of measured κ and D caused by τ_L is calculated as $\%\Delta\kappa/\kappa$ and $\%\Delta D/D$, respectively and is shown in inset of Fig. 10(b). Note that κ and D in denominator are measured values for 13 nm-thick sample as indicated in Table 4. $\%\Delta\kappa/\kappa$ is less than 2% for all τ_L values which solidify our claim that laser absorption coefficient has negligible effect on κ measurement. Regarding $\%\Delta D/D$, it

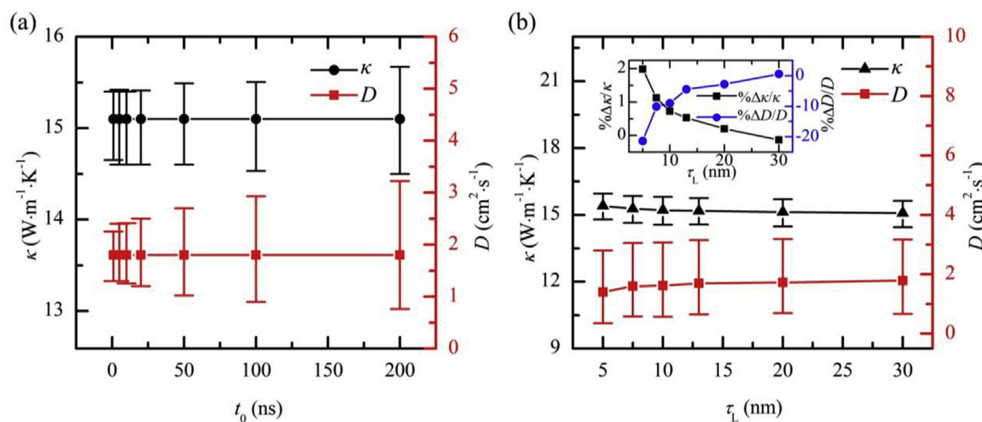

Fig. 10. (a) Effect of laser pulse width on measurement accuracy. Uncertainty of κ (left vertical axis) and D (right vertical axis) are calculated against different t_0 values. In this calculation the absolute value of κ and D are fixed and equal to the determined values. The uncertainty of determined D is more sensitive to t_0 than that of κ. For example, as t_0 changes from 200 ns to 50 ns, the uncertainty of D decreases by more than 40%, while the uncertainty of κ decreases by less than 20%. (b) Effect of laser absorption depth on κ (left vertical axis) and D (right vertical axis). The inset shows the percentage error of κ and D determined caused by τ_L variation. When τ_L is more than sample thickness (13 nm), its effect on κ and D is negligible. However, while τ_L is extremely small it can have considerable effect on our measurement, especially D determination. Also, It shows that over a wide range of τ_L, uncertainties remain constant.

could be considerable when τ_L is much smaller than its actual value. This uncertainty is caused by uniform ΔN assumption in the thickness direction that is made in our 3D numerical simulation. Physically, as τ_L decreases, ΔN increases within the top layer of sample with a thickness equal to τ_L, leading to a hot carrier diffusion diminution in all domain. To evaluate the accuracy of our technique, here we consider 20% error in τ_L measurement. In this case, the uncertainty caused by this error is less than 0.3% and 4% in κ and D, respectively. It means that for few-layered samples and monolayers, τ_L has almost no effect on D and κ measurements.

6.4. *Effect of sample thickness on measurement*

To shed light on effect of sample thickness on our measurement accuracy, κ and D for several arbitrary thicknesses are calculated, as shown in Fig. 11. In this study, we calculate the temperature rise of different arbitrary samples with thickness in range 10–100 nm. Fig. 11(a) shows the temperature rise of these samples with different thicknesses under three heating states (left vertical axis) as well as Θ values (right vertical axis) when κ and D are fixed as 15.1 W m^{-1} K^{-1} and 1.78 cm^2 s^{-1} in calculation. It is perfectly clear that as the thickness decreases, the temperature rise increases for all three heating states, while Θ_{20} and Θ_{100} remain almost unchanged. This shows that our relative temperature rise calculation is independent of film's thickness. As shown in Fig. 11(b), we obtain κ (left vertical axis) and D (right vertical axis) of these arbitrary samples using the 3D numerical calculations introduced in Fig. 11(a) and experimental values of Θ for the 13 nm sample. Fig. 11(b) shows that κ remains almost unchanged with increased thickness, while D for thicker arbitrary sample is more than thinner ones. Additionally, the uncertainty of measured κ and D are plotted in Fig. 11(b) and it is obvious from that by changing the thickness, the uncertainty of κ and D do not change significantly. The inset of Fig. 11(b) shows the percentage variation of κ (left vertical axis) and D (right vertical axis) caused by film's thickness variation. This deviation is calculated as $\%\Delta\kappa/\kappa$ and $\%\Delta D/D$, where $\Delta\kappa$ (or ΔD) is the difference between determined κ (or D) of each arbitrary sample and actual value of κ (or D) of 13 nm-thick sample as reported in

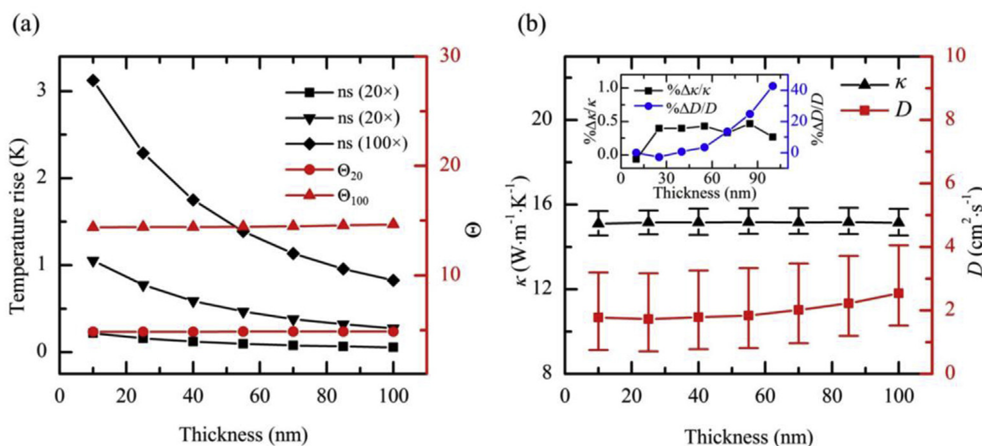

Fig. 11. (a) Temperature rise (left vertical axis) and Θ (right vertical axis) are calculated using our 3D numerical model for several thicknesses in a range of 10–100 nm. As thickness increases, the temperature rise under all heating states decreases, while the Θ values changes very little. (b) Calculated κ (left vertical axis) and D (right vertical axis) under different arbitrary thicknesses. The inset shows the percentage error caused by errors in thickness measurement. It is obvious that these thickness errors have almost no effect on κ measurement. Also, determined D increases with increased thickness. $\%\Delta D/D$ is only less than 20% while the error of thickness measurement is extremely large and is around 400%. Additionally, it is clear that the uncertainty of these two parameters for each arbitrary sample varies very little among different thicknesses.

Table 4. This study evaluates the effects of thickness measurement on nET-Raman technique. Again, as mentioned in previous section, $\%\Delta D/D$ is caused by uniform ΔN assumption in cross-plane direction in our simulation. From the inset of Fig. 11(b) we can conclude that thickness measurement has almost no effect on κ measurement. Also, even when the sample thickness was measured as 60 nm which means more 300% error in thickness measurement, it could cause only 5% error in determined D value. Therefore, we can conclude that film's thickness measurement has very little effect on our technique. This shows another significant capability of nET-Raman technique in improving experimental accuracies.

6.5. *Effect of laser spot position*

As mentioned in section 3, the sample is placed on a 3D nano-stage. Normally, during the time that we perform the experiment, this stage has very slight drift in the in-plane directions. Due to these drifts, laser spot location on the sample will be changed a little bit. The results which are reported in Table 4 are determined based on this assumption that laser spot under different heating states is exactly located at the center of suspended sample. For the suspended samples, since the heating area is strongly restricted to the suspended area, these changes of laser spot location could cause considerable amount of uncertainty in final results in any Raman study. In our technique, since we irradiate the WS_2 thin films under three different states, we need to consider each of them in this study. First, using our 3D numerical model, the Raman average temperature rise (ΔT in Fig. 12) of the 13-nm sample under each of these three states is calculated for different laser spot locations. Fig. 12 shows the sample under laser irradiation for these three cases. Laser spots are similar to the experimental values as presented in Table 1. In Fig. 12, δ indicates the laser spot shift from the center of sample and it varies from 0 to 2.5 µm. As δ increases from zero to 2.5 µm, ΔT for all three cases decreases, as it is expected. This temperature drop is more significant in steady state (CW) case. As mentioned earlier in section 2, under CW laser irradiation, heat diffusion length is equal to the size of suspended area, while under pulsed laser it is less than that. Therefore, CW case is more sensitive to effect of laser spot position shift than ns cases.

Among two ns cases, the one under 100 × is not sensitive to the laser spot location. Therefore, here we only study the effect of laser spot drift under CW laser and ns laser with 20 × objective. To do so, we define two new normalized temperature values as: $\Theta'_{20} = \Delta T_{ns20}/\Delta T_{CW20}$ and $\Theta'_{100} = \Delta T_{ns100}/\Delta T_{CW20}$.

In this study, these two theoretically calculated normalized temperature values work similar to experimental Θ_{20} and Θ_{100}. Using Θ'_{20} and Θ'_{100} of different laser positions with 3% uncertainty assumption for each of them, we can find new κ_d and D_d values. Θ'_{100} only depends on ΔT_{CW20}, while Θ'_{20} depends on both ΔT_{ns20} and ΔT_{CW20}. Each Θ'_{20} (or Θ'_{100}) represents a contour line similar to Fig. 7(a) and (b). As a result, we can find the effect of laser spot position by comparing Θ'_{20} (or Θ'_{100}) with Θ_{20} (or Θ_{100}) that were introduced in previous sections. To do this comparison, deviation of Θ'_{20} from Θ_{20} is calculated as $|1 - \Theta'_{20}/\Theta_{20}| \times 100$, and is plotted as contour in Fig. 13. While laser spot position under each of

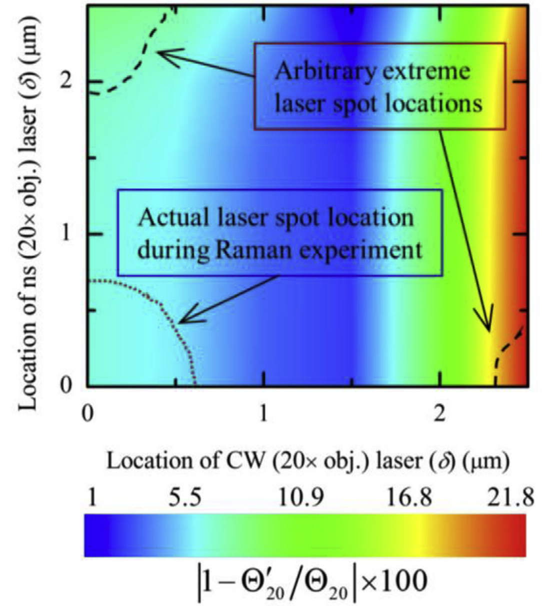

Fig. 13. The percentage error caused by laser spot position shift in Θ. This error could be significant when either ns spot is at maximum distance from center and CW spot is located at center (dashed line in upper left corner), or CW spot is located at maximum distance from center and ns spot is fixed at center (dashed line in lower right corner). Note that red dotted line indicates the actual laser spot area during our Raman experiment. (For interpretation of the references to colour in this figure legend, the reader is referred to the Web version of this article.)

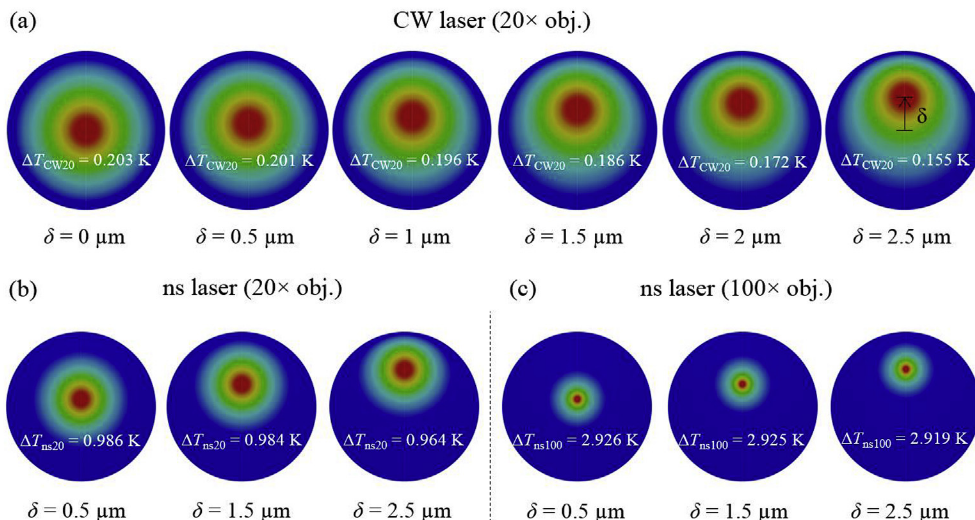

Fig. 12. 13 nm-thick sample is irradiated by (a) CW laser under 20 × objective lens, (b) ns laser under 20 × objective lens, and (c) ns laser under 100 × objective lens, respectively, at different laser spot positions. δ represents the laser spot distance from the sample center. Raman averaged temperature (ΔT) is calculated for each case and shown in the figure.

Table 5
Measured κ_d, D_d, and percentage error of each of them based on different locations of laser spot.

Scenario		κ_d (W·m^{-1}·K^{-1})	D_d (cm^2·s^{-1})	% $\lvert\Delta\kappa/\kappa\rvert$	% $\lvert\Delta D/D\rvert$
1–1	$\delta_{CW20} = 0$ μm $\delta_{ns20} = 1.5$ μm	$15.0^{+0.4}_{-0.5}$	$1.71^{+0.68}_{-0.64}$	0.3	3.9
1–2	$\delta_{CW20} = 0$ μm $\delta_{ns20} = 2.5$ μm	$14.6^{+0.6}_{-0.6}$	$1.31^{+0.84}_{-0.69}$	2.9	26.4
2–1	$\delta_{CW20} = 1.5$ μm $\delta_{ns20} = 0$ μm	$17.4^{+0.9}_{-0.7}$	$0.18^{+0.77}_{-0.18}$	15.7	91.6
2–2	$\delta_{CW20} = 2.5$ μm $\delta_{ns20} = 0$ μm	~24	–	~60	–

these states changes from 0 to 2.5 μm, the percentage error calculated above is maximized when laser spot is located at the center under ns case and is shifted 2.5 μm from the center under CW case. The other scenario that we explore here is when the CW laser spot remains at the center of suspended film, while δ is 2.5 μm under ns laser irradiation. These two scenarios are indicated in Fig. 13 by black dashed lines. Based on this introduction, κ_d and D_d are calculated for these two scenarios. It should be noted that to maximize the stability of 3D stage and minimize the laser spot drift during our Raman experiment, we wait for an appropriate time (hours) until the stage becomes very stable. After this time, laser spot drifts under three states is much less and is in the approximate range that is shown in Fig. 13 by red dotted line. Therefore, it should be noted that just mentioned study evaluates the extreme cases, and not the real case which is much more stable and accurate. Table 5 shows the results of this study.

Regarding Table 5, under scenarios 1-1 and 1–2 κ_d and D_d do not change significantly in comparison to the normal case that spot is located at the center. This is reasonable since Raman average temperature rise does not change a lot with drift of the laser spot under ns laser. Also, last two columns of Table 5 indicate the percentage error of these calculations by comparing them with the values determined for the 13 nm sample in section 5, as $|\Delta\kappa/\kappa| = |(\kappa-\kappa_d)/\kappa|$ and $|\Delta D/D| = |(D - D_d)/D|$, respectively. It should be noted that under the first two scenarios Θ'_{100} remains unchanged. Under scenarios 2–1 and 2-2 in which locations of ns laser spots are held at center and δ_{CW20} varies, κ_d and D_d change significantly. In fact, in case 2–1 when the laser spot shift is 30% of the sample radius, the error caused by this drift in κ_d and D_d is around 16% and 92%, respectively. Under case 2-2, it is not possible to determine D_d, since there is no cross-point for two contour lines. As shown in Fig. 7(c), we extract two lines from two contours and their cross point gives the κ_d and D_d values simultaneously. When laser spot position under CW laser is far from the center, the constant Θ'_{100} contour lines [similar to Fig. 7(b)] will be less sensitive to κ. However, since Θ'_{20} (or Θ_{20}) is almost independent of D_d, we can roughly estimate κ_d. In summary, we conclude that our experiment is more sensitive to location of CW laser spot than ns laser spot.

7. Conclusion

In this work, a nET-Raman technique was designed and employed successfully for measuring in-plane thermal conductivity (κ) and hot carrier diffusion coefficient (D) of suspended WS_2 thin films with thicknesses in a range of 13–107 nm. Using this technique, hot carrier and thermal transport of these samples were characterized without need of Raman temperature calibration and laser absorption coefficient which are the main sources of errors in steady state Raman studies. In contrast to electrical techniques, nET-Raman is a non-contact method. In this technique, samples were irradiated by two different lasers: continuous wave (CW) and nanosecond (ns). These two lasers are used to heat the samples and extract Raman signals under different heating spot sizes. As the heating spot size decreases, the effect of hot carrier diffusion coefficient becomes more significant. By analyzing the experimental data, we could determine Raman power coefficient under each heating state and by developing a 3D physical model, κ and D of four WS_2 samples were determined. The thermal conductivity was observed to increase from $15.1^{+0.3}_{-0.4}$ to $38.8^{+2.6}_{-2.4}$ W·m^{-1} K^{-1} as the sample thickness increased from 13 nm to 107 nm. This effect was attributed to stronger effect of surface scattering for thinner films. Also, hot carrier diffusion coefficient values were around to 2 cm^2·s^{-1} for majority of the samples, except the thickest one. This trend was explained by the constant lattice scattering, and these samples are suspended and consequently independent of effects of substrate. For the 107 nm sample, the higher D value was attributed to better structure of WS_2 layers for this sample that might be caused by the exfoliation method. In addition to κ and D, hot carrier diffusion length (Δr_{HC}) and carrier mobility (μ) of each sample were determined. A detailed discussion was provided about the scope of this technique and different parameters that could affect the measurement uncertainty, including sample's thickness, laser absorption level, and laser spot position.

Conflicts of interest

All authors have no competing interests to declare.

Acknowledgement

Partial support of this work by the College of Engineering of Iowa State University is gratefully acknowledged.

References

[1] A.J. Mannix, B. Kiraly, M.C. Hersam, N.P. Guisinger, Synthesis and chemistry of elemental 2D materials, Nat. Rev. Chem. 1 (2017) 0014.
[2] E. Pop, V. Varshney, A.K. Roy, Thermal properties of graphene: fundamentals and applications, MRS Bull. 37 (2012) 1273–1281.
[3] Y. Xie, M. Han, R. Wang, H. Zobeiri, X. Deng, P. Zhang, X. Wang, Graphene aerogel based bolometer for ultrasensitive sensing from ultraviolet to far-infrared, ACS Nano 13 (2019) 5385–5396.
[4] Q.-Y. Li, K. Xia, J. Zhang, Y. Zhang, Q. Li, K. Takahashi, X. Zhang, Measurement of specific heat and thermal conductivity of supported and suspended graphene by a comprehensive Raman optothermal method, Nanoscale 9 (2017) 10784–10793.
[5] Q.-Y. Li, K. Takahashi, H. Ago, X. Zhang, T. Ikuta, T. Nishiyama, K. Kawahara, Temperature dependent thermal conductivity of a suspended submicron graphene ribbon, J. Appl. Phys. 117 (2015) 065102.
[6] Q.-Y. Li, X. Zhang, K. Takahashi, Variable-spot-size laser-flash Raman method to measure in-plane and interfacial thermal properties of 2D van der Waals heterostructures, Int. J. Heat Mass Transf. 125 (2018) 1230–1239.
[7] A. Ramasubramaniam, D. Naveh, E. Towe, Tunable band gaps in bilayer transition-metal dichalcogenides, Phys. Rev. B 84 (2011) 205325.
[8] T. Chu, H. Ilatikhameneh, G. Klimeck, R. RahWman, Z. Chen, Electrically tunable bandgaps in bilayer MoS_2, Nano Lett. 15 (2015) 8000–8007.
[9] H. Nan, Z. Wang, W. Wang, Z. Liang, Y. Lu, Q. Chen, D. He, P. Tan, F. Miao, X. Wang, Strong photoluminescence enhancement of MoS_2 through defect engineering and oxygen bonding, ACS Nano 8 (2014) 5738–5745.
[10] A. Hanbicki, M. Currie, G. Kioseoglou, A. Friedman, B. Jonker, Measurement of high exciton binding energy in the monolayer transition-metal

dichalcogenides WS_2 and WSe_2, Solid State Commun. 203 (2015) 16–20.
[11] M.-L. Tsai, S.-H. Su, J.-K. Chang, D.-S. Tsai, C.-H. Chen, C.-I. Wu, L.-J. Li, L.-J. Chen, J.-H. He, Monolayer MoS_2 heterojunction solar cells, ACS Nano 8 (2014) 8317–8322.
[12] X. Yang, W. Fu, W. Liu, J. Hong, Y. Cai, C. Jin, M. Xu, H. Wang, D. Yang, H. Chen, Engineering crystalline structures of two-dimensional MoS_2 sheets for high-performance organic solar cells, J. Mater. Chem. 2 (2014) 7727–7733.
[13] Z. Zheng, T. Zhang, J. Yao, Y. Zhang, J. Xu, G. Yang, Flexible, transparent and ultra-broadband photodetector based on large-area WSe_2 film for wearable devices, Nanotechnology 27 (2016) 225501.
[14] C. Xie, C. Mak, X. Tao, F. Yan, Photodetectors based on two-dimensional layered materials beyond graphene, Adv. Funct. Mater. 27 (2017) 1603886.
[15] V. Podzorov, M. Gershenson, C. Kloc, R. Zeis, E. Bucher, High-mobility field-effect transistors based on transition metal dichalcogenides, Appl. Phys. Lett. 84 (2004) 3301–3303.
[16] S. Larentis, B. Fallahazad, E. Tutuc, Field-effect transistors and intrinsic mobility in ultra-thin $MoSe_2$ layers, Appl. Phys. Lett. 101 (2012) 223104.
[17] H. Lin, S. Xu, Y.-Q. Zhang, X. Wang, Electron transport and bulk-like behavior of Wiedemann–Franz law for sub-7 nm-thin iridium films on silkworm silk, ACS Appl. Mater. Interfaces 6 (2014) 11341–11347.
[18] J.H. Strait, P. Nene, F. Rana, High intrinsic mobility and ultrafast carrier dynamics in multilayer metal-dichalcogenide MoS_2, Phys. Rev. B 90 (2014) 245402.
[19] W. Bao, X. Cai, D. Kim, K. Sridhara, M.S. Fuhrer, High mobility ambipolar MoS_2 field-effect transistors: substrate and dielectric effects, Appl. Phys. Lett. 102 (2013) 042104.
[20] G. Nazir, M.F. Khan, V.M. Iermolenko, J. Eom, Two-and four-probe field-effect and Hall mobilities in transition metal dichalcogenide field-effect transistors, RSC Adv. 6 (2016) 60787–60793.
[21] A.D. Semenov, G.N. Gol'tsman, R. Sobolewski, Hot-electron effect in superconductors and its applications for radiation sensors, Supercond. Sci. Technol. 15 (2002) R1.
[22] X. Shen, H. Wang, T. Yu, How do the electron beam writing and metal deposition affect the properties of graphene during device fabrication? Nanoscale 5 (2013) 3352–3358.
[23] S. Kang, H.C. Movva, A. Sanne, A. Rai, S.K. Banerjee, Influence of electron-beam lithography exposure current level on the transport characteristics of graphene field effect transistors, J. Appl. Phys. 119 (2016) 124502.
[24] N. Kumar, J. He, D. He, Y. Wang, H. Zhao, Charge carrier dynamics in bulk MoS_2 crystal studied by transient absorption microscopy, J. Appl. Phys. 113 (2013) 133702.
[25] R. Wang, B.A. Ruzicka, N. Kumar, M.Z. Bellus, H.-Y. Chiu, H. Zhao, Ultrafast and spatially resolved studies of charge carriers in atomically thin molybdenum disulfide, Phys. Rev. B 86 (2012) 045406.
[26] J. He, D. He, Y. Wang, Q. Cui, F. Ceballos, H. Zhao, Spatiotemporal dynamics of excitons in monolayer and bulk WS_2, Nanoscale 7 (2015) 9526–9531.
[27] P. Yuan, J. Liu, R. Wang, X. Wang, The hot carrier diffusion coefficient of sub-10 nm virgin MoS_2: uncovered by non-contact optical probing, Nanoscale 9 (2017) 6808–6820.
[28] P. Yuan, R. Wang, H. Tan, T. Wang, X. Wang, Energy transport state resolved Raman for probing interface energy transport and hot carrier diffusion in few-layered MoS_2, ACS Photonics 4 (2017) 3115–3129.
[29] P. Yuan, R. Wang, T. Wang, X. Wang, Y. Xie, Nonmonotonic thickness-dependence of in-plane thermal conductivity of few-layered MoS_2: 2.4 to 37.8 nm, Phys. Chem. Chem. Phys. 20 (2018) 25752–25761.
[30] R. Wang, T. Wang, H. Zobeiri, P. Yuan, C. Deng, Y. Yue, S. Xu, X. Wang, Measurement of thermal conductivity of suspended MoS_2 and $MoSe_2$ by nanosecond ET-Raman free of temperature calibration and laser absorption evaluation, Nanoscale 10 (2018) 23087–23102.
[31] R. Wang, H. Zobeiri, H. Lin, W. Qu, X. Bai, C. Deng, X. Wang, Anisotropic thermal conductivities and structure in lignin-based microscale carbon fibers, Carbon 147 (2019) 58–69.
[32] A. Fan, Y. Hu, W. Ma, H. Wang, X. Zhang, Dual-wavelength laser flash Raman spectroscopy method for in-situ measurements of the thermal diffusivity: principle and experimental verification, J. Therm. Sci. 28 (2018) 159–168.
[33] N. Peimyoo, J. Shang, W. Yang, Y. Wang, C. Cong, T. Yu, Thermal conductivity determination of suspended mono-and bilayer WS_2 by Raman spectroscopy, Nano Res. 8 (2015) 1210–1221.
[34] R. Yan, J.R. Simpson, S. Bertolazzi, J. Brivio, M. Watson, X. Wu, A. Kis, T. Luo, A.R. Hight Walker, H.G. Xing, Thermal conductivity of monolayer molybdenum disulfide obtained from temperature-dependent Raman spectroscopy, ACS Nano 8 (2014) 986–993.
[35] S. Sahoo, A.P. Gaur, M. Ahmadi, M.J.-F. Guinel, R.S. Katiyar, Temperature-dependent Raman studies and thermal conductivity of few-layer MoS_2, J. Phys. Chem. C 117 (2013) 9042–9047.
[36] H.R. Gutiérrez, N. Perea-López, A.L. Elías, A. Berkdemir, B. Wang, R. Lv, F. López-Urías, V.H. Crespi, H. Terrones, M. Terrones, Extraordinary room-temperature photoluminescence in triangular WS_2 monolayers, Nano Lett. 13 (2012) 3447–3454.
[37] Z. Jin, X. Li, J.T. Mullen, K.W. Kim, Intrinsic transport properties of electrons and holes in monolayer transition-metal dichalcogenides, Phys. Rev. B 90 (2014), 04542δns20 = 0 μm 2.
[38] A.L. Elías, N. Perea-Lopez, A. Castro-Beltran, A. Berkdemir, R. Lv, S. Feng, A.D. Long, T. Hayashi, Y.A. Kim, M. Endo, Controlled synthesis and transfer of large-area WS_2 sheets: from single layer to few layers, ACS Nano 7 (2013) 5235–5242.
[39] W.S. Yun, S. Han, S.C. Hong, I.G. Kim, J. Lee, Thickness and strain effects on electronic structures of transition metal dichalcogenides: 2H-MX_2 semiconductors (M= Mo, W; X= S, Se, Te), Phys. Rev. B 85 (2012) 033305.
[40] H. Wang, C. Zhang, F. Rana, Ultrafast dynamics of defect-assisted electron–hole recombination in monolayer MoS_2, Nano Lett. 15 (2014) 339–345.
[41] M. Palummo, M. Bernardi, J.C. Grossman, Exciton radiative lifetimes in two-dimensional transition metal dichalcogenides, Nano Lett. 15 (2015) 2794–2800.
[42] N.B. Mohamed, H.E. Lim, F. Wang, S. Koirala, S. Mouri, K. Shinokita, Y. Miyauchi, K. Matsuda, Long radiative lifetimes of excitons in monolayer transition-metal dichalcogenides MX_2 (M= Mo, W; X= S, Se), APEX 11 (2017) 015201.
[43] P. O'hare, W. Hubbard, G. Johnson, H. Flotow, Calorimetric measurements of the low-temperature heat capacity, standard molar enthalpy of formation at 298.15 K, and high-temperature molar enthalpy increments relative to 298.15 K of tungsten disulfide (WS_2), and the thermodynamic properties to 1500 K, J. Chem. Thermodyn. 16 (1984) 45–59.
[44] C. Christofides, A. Othonos, E. Loizidou, Influence of temperature and modulation frequency on the thermal activation coupling term in laser photothermal theory, J. Appl. Phys. 92 (2002) 1280–1285.
[45] M. Nestoros, B.C. Forget, C. Christofides, A. Seas, Photothermal reflection versus temperature: quantitative analysis, Phys. Rev. B 51 (1995) 14115.
[46] C. Christofides, F. Diakonos, A. Seas, C. Christou, M. Nestoros, A. Mandelis, Two-layer model for photomodulated thermoreflectance of semiconductor wafers, J. Appl. Phys. 80 (1996) 1713–1725.
[47] P. Jiang, X. Qian, X. Gu, R. Yang, Probing anisotropic thermal conductivity of transition metal dichalcogenides MX_2 (M= Mo, W and X= S, Se) using time-domain thermoreflectance, Adv. Mater. 29 (2017) 1701068.
[48] H.-L. Liu, C.-C. Shen, S.-H. Su, C.-L. Hsu, M.-Y. Li, L.-J. Li, Optical properties of monolayer transition metal dichalcogenides probed by spectroscopic ellipsometry, Appl. Phys. Lett. 105 (2014) 201905.
[49] S. Alfihed, M. Hossain, A. Alharbi, A. Alyamani, F.H. Alharbi, PLD grown polycrystalline tungsten disulphide (WS_2) films, J. Mater. (2013) 2013.
[50] H.-C. Kim, H. Kim, J.-U. Lee, H.-B. Lee, D.-H. Choi, J.-H. Lee, W.H. Lee, S.H. Jhang, B.H. Park, H. Cheong, Engineering optical and electronic properties of WS_2 by varying the number of layers, ACS Nano 9 (2015) 6854–6860.
[51] W. Tang, S. Rassay, N. Ravindra, Electronic & Optical properties of transition-metal dichalcogenides 2 (2017) 59–65.
[52] E. Marín, Characteristic dimensions for heat transfer, Latin-Am. J. Phys. Educ. 4 (2010) 56–60.
[53] C. Wu, D. Wittry, Investigation of minority-carrier diffusion lengths by electron bombardment of Schottky barriers, J. Appl. Phys. 49 (1978) 2827–2836.
[54] H. Zobeiri, R. Wang, T. Wang, H. Lin, C. Deng, X. Wang, Frequency-domain energy transport state-resolved Raman for measuring the thermal conductivity of suspended nm-thick $MoSe_2$, Int. J. Heat Mass Transf. 133 (2019) 1074–1085.
[55] A. Berkdemir, H.R. Gutiérrez, A.R. Botello-Méndez, N. Perea-López, A.L. Elías, C.-I. Chia, B. Wang, V.H. Crespi, F. López-Urías, J.-C. Charlier, Identification of individual and few layers of WS_2 using Raman Spectroscopy, Sci. Rep. 3 (2013) 1755.
[56] H. Li, J. Wu, Z. Yin, H. Zhang, Preparation and applications of mechanically exfoliated single-layer and multilayer MoS_2 and WSe_2 nanosheets, Acc. Chem. Res. 47 (2014) 1067–1075.
[57] R. Cuscó, E. Alarcón-Lladó, J. Ibanez, L. Artús, J. Jimenez, B. Wang, M.J. Callahan, Temperature dependence of Raman scattering in ZnO, Phys. Rev. B 75 (2007) 165202.
[58] Y. Yue, G. Eres, X. Wang, L. Guo, Characterization of thermal transport in micro/nanoscale wires by steady-state electro-Raman-thermal technique, Appl. Phys. A 97 (2009) 19–23.
[59] K.G. Zhou, M. Zhao, M.J. Chang, Q. Wang, X.Z. Wu, Y. Song, H.L. Zhang, Size-dependent nonlinear optical properties of atomically thin transition metal dichalcogenide nanosheets, Small 11 (2015) 694–701.
[60] K. Wang, Y. Feng, C. Chang, J. Zhan, C. Wang, Q. Zhao, J.N. Coleman, L. Zhang, W.J. Blau, J. Wang, Broadband ultrafast nonlinear absorption and nonlinear refraction of layered molybdenum dichalcogenide semiconductors, Nanoscale 6 (2014) 10530–10535.
[61] Y.-Y. Chen, M. Gholipour, D. Chen, Flexible transition metal dichalcogenide field-effect transistors: a circuit-level simulation study of delay and power under bending, process variation, and scaling, in: Design Automation Conference (ASP-DAC), 2016 21st Asia and South Pacific, IEEE, 2016, pp. 761–768.
[62] A.N. Gandi, U. Schwingenschlögl, WS_2 as an excellent high-temperature thermoelectric material, Chem. Mater. 26 (2014) 6628–6637.
[63] D.A. Neamen, Semiconductor Physics and Devices: Basic Principles, McGraw-Hill, New York, NY, 2012.
[64] A. Einstein, Über die von der molekularkinetischen Theorie der Wärme geforderte Bewegung von in ruhenden Flüssigkeiten suspendierten Teilchen, Ann. Phys. 322 (1905) 549–560.
[65] X. Liu, J. Hu, C. Yue, N. Della Fera, Y. Ling, Z. Mao, J. Wei, High performance field-effect transistor based on multilayer tungsten disulfide, ACS Nano 8 (2014) 10396–10402.
[66] D. Ovchinnikov, A. Allain, Y.-S. Huang, D. Dumcenco, A. Kis, Electrical transport properties of single-layer WS_2, ACS Nano 8 (2014) 8174–8181.
[67] W. Sik Hwang, M. Remskar, R. Yan, V. Protasenko, K. Tahy, S. Doo Chae,

P. Zhao, A. Konar, H. Xing, A. Seabaugh, Transistors with chemically synthesized layered semiconductor WS_2 exhibiting 105 room temperature modulation and ambipolar behavior, Appl. Phys. Lett. 101 (2012) 013107.
[68] D. Braga, I. Gutiérrez Lezama, H. Berger, A.F. Morpurgo, Quantitative determination of the band gap of WS_2 with ambipolar ionic liquid-gated transistors, Nano Lett. 12 (2012) 5218–5223.
[69] B. Peng, H. Zhang, H. Shao, Y. Xu, X. Zhang, H. Zhu, Thermal conductivity of monolayer MoS_2, $MoSe_2$, and WS_2: interplay of mass effect, interatomic bonding and anharmonicity, RSC Adv. 6 (2016) 5767–5773.
[70] G.A. Slack, Nonmetallic crystals with high thermal conductivity, J. Phys. Chem. Solids 34 (1973) 321–335.
[71] M.-W. Lin, I.I. Kravchenko, J. Fowlkes, X. Li, A.A. Puretzky, C.M. Rouleau, D.B. Geohegan, K. Xiao, Thickness-dependent charge transport in few-layer MoS_2 field-effect transistors, Nanotechnology 27 (2016) 165203.
[72] S. Das, H.-Y. Chen, A.V. Penumatcha, J. Appenzeller, High performance multilayer MoS_2 transistors with scandium contacts, Nano Lett. 13 (2012) 100–105.
[73] S.-L. Li, K. Wakabayashi, Y. Xu, S. Nakaharai, K. Komatsu, W.-W. Li, Y.-F. Lin, A. Aparecido-Ferreira, K. Tsukagoshi, Thickness-dependent interfacial coulomb scattering in atomically thin field-effect transistors, Nano Lett. 13 (2013) 3546–3552.
[74] S. Chen, Q. Li, Q. Zhang, Y. Qu, H. Ji, R.S. Ruoff, W. Cai, Thermal conductivity measurements of suspended graphene with and without wrinkles by micro-Raman mapping, Nanotechnology 23 (2012) 365701.
[75] Q.-Y. Li, X. Zhang, Y.-D. Hu, Laser flash Raman spectroscopy method for thermophysical characterization of 2D nanomaterials, Thermochim. Acta 592 (2014) 67–72.